Unravelling the Impact of Porosity on Water Stability of Porous Bi(III) Halide Semiconductors and their Potential for Red Tide Mitigation

Ali Azmy,[1,#] Alissa Brooke Anderson,[1,#] Anamika Mishra,[1] Enlin Lo,[2] Neelam Tariq,[1] Ioannis N. Gkikas,[1] Brandon Sauval,[1] Nicholas Giunto,[1] Amrit Kaur,[1] Stephanie Krzypkowski,[1] Nourdine Zibouche,[3] George P. Philippidis[4] and Ioannis Spanopoulos*,[1]

[1]*Department of Chemistry, University of South Florida, Tampa, Florida 33620, USA*

[2]*Department of Molecular Biosciences, University of South Florida, Tampa, Florida 33620, USA*

[3]*Department of Chemistry, University of Lancaster, Lancaster, LA1 4YW, UK*
[4]*Department of Integrative Biology and Patel College of Global Sustainability, University of South Florida, Tampa, Florida 33620, USA*

ABSTRACT

We recently developed a family of materials, Porous Metal Halide Semiconductors (PMHS), that exhibit record water stability and tunable optoelectronic properties. However, the extent to which porosity influences these features remains unclear. Motivated by this, we report the synthesis of (DHT)$(H_3O)_2Bi_4I_{16}\cdot 2(H_2O)$ (DHT = [3.3.3] cryptand), where the custom-made DHT cage expands the pore size from 4.3 to 6.2 Å, compared to previously reported DHS-based analogs (DHS = [2.2.2] cryptand). The material has been water stable for 24 months, featuring a single crystal to single crystal transformation, while gas and vapor sorption studies demonstrated that it can selectively adsorb and desorb H_2O at 298K. (DHT)$(H_3O)_2Bi_4I_{16}\cdot 2(H_2O)$ is a direct bandgap semiconductor that exhibits broad band-edge emission at room temperature. This combination of attributes prompted us to evaluate the material against *Karenia brevis*, an alga responsible for harmful algal blooms (HABs). Our studies revealed that (DHT)$(H_3O)_2Bi_4I_{16}\cdot 2(H_2O)$ suppressed *K. brevis* growth at concentrations as low as 10 mg/L, with no inhibition observed against non-target marine algae strains. This work elucidates the influence of porosity on the optoelectronic properties and water stability of PMHS compounds, and underscores their potential for impactful, previously unexplored applications such as HAB mitigation.

INTRODUCTION

Hybrid (organic-inorganic) metal halide semiconductors (MHS) is a family of materials with unique structural versatility and fully customizable mechanical,[1] magnetic and optoelectronic properties.[2-4] The adjustable composition of the inorganic part and the tailor-made design of the organic part of the structure allow them to be utilized not only for established semiconductor applications, such as solar cells[5-6] and photodetectors,[7-8] but also for emerging applications, such as gas sensing,[9] spin valves[10] and antibacterial coatings.[11]

Evidently, two of the most important prerequisites for commercialization are the non-toxic nature of the materials and their long-term environmental stability.[12] Despite significant efforts to create lead-free, water-stable MHS,[13-14] a permanent solution remained elusive until recently. Motivated by the above challenges, we created a family of materials, namely porous metal halide semiconductors (PMHS).[15] The use of molecular cages as structure-directing agents and counter-cations not only rendered reported PMHS porous but also water-stable for 27 months so far, a record stability performance for MHS.[16]

Despite this achievement, the extent to which porosity dictates water stability in PMHS materials is unclear. In an effort to investigate this relationship, we report here a member of the family of PMHS compounds, namely (DHT)$(H_3O)_2Bi_4I_{16}\cdot 2(H_2O)$, (DHT = [3.3.3] cryptand), to study the effect of porous nature on the optoelectronic properties and water stability of isostructural PMHS compounds. The material has been water stable for 24 months so far based on XRD studies, featuring a single crystal to single crystal (SCSC) transformation in water, while gas and vapor sorption studies demonstrated that it can selectively adsorb and desorb H_2O at room temperature (RT), while it is impermeable to N_2 and CO_2. In addition to its robust porosity and selective sorption behavior, the compound is a direct bandgap semiconductor with broad band-edge emission at room temperature, characteristics closely resembling those of its previously reported analog, (DHS)Bi_2I_8 (DHS = [2.2.2] cryptand).[17] Notably, (DHS)Bi_2I_8 not only exhibits similar water stability but also demonstrates broad-spectrum antibacterial activity against both Gram-positive and Gram-negative bacteria. This convergence of water stability, porosity, and bioactivity positions PMHS materials as promising candidates for environmental remediation applications.

Motivated by these multifunctional characteristics, we investigated the potential of PMHS compounds for mitigating harmful algal blooms (HABs). In recent years, the

frequency, intensity, and geological distribution of HABs have increased, posing heightened risks to marine ecosystems and human health.[18] *Karenia brevis* (*K. brevis*) is a toxic dinoflagellate commonly associated with the "red tide" blooms that produces potent neurotoxins known as brevetoxins (BTx).[19] These toxins can have detrimental effects on marine life, leading to fish kills, marine mammal strandings, and disruptions to the food web.[20] Additionally, when these BTx become aerosolized, they pose significant risks to human health, causing respiratory irritation and exacerbating conditions such as asthma.[21] The economic impacts of *K. brevis* blooms on coastal communities are also considerable, often necessitating the closure of shellfish harvesting areas and causing substantial losses for coastal tourism and fisheries industries.[22]

For these reasons, multiple HAB mitigation strategies have been implemented focusing on biological, physical or chemical methods. Biological techniques employ top-down grazing and bottom-up bacterial decomposition through the use of parasites, copepods, and ciliates.[23-24] However, there are limitations to their widespread utilization due to hurdles associated with the mass production, storage, and controlled deployment of proposed organisms. Physical treatments of HABs involve the removal of harmful algae cells using methods such as skimming, isolation, and ultrasonic destruction.[25-26] Although generally safe and effective, such treatments are expensive, with limited effectiveness in large-scale blooms, and often lack selectivity for HAB species. Chemical-based methods are the most extensively studied approaches for managing HAB blooms, including algicides such as copper sulfate, ozone, sodium hypochlorite, and magnesium hydroxide.[27-28] Although chemical methods are effective in most cases, concerns exist regarding their impact on non-target organisms, bioaccumulation, and potential uncontrolled release into the environment.

Considering that current mitigation strategies are still relatively ineffective against HABs, there is a pressing need to test alternative solutions.[29] Recognizing that chemical methods are more efficient and versatile, we hypothesized that a material capable of selectively mitigating HABs without uncontrolled release to the environment and with minimal to no impact on phytoplankton and marine organisms would be an excellent candidate for this application.

In this regard, water-stable PMHS materials hold great promise, as they feature fine-tunable optical properties, are composed of abundant, inexpensive, and biocompatible elements, such as Bi and I, and can be activated with visible light to

generate reactive oxygen species (ROS).[15, 17] Water stability, meaning PMHS are water-insoluble, is critical because, in contrast to currently utilized water-soluble inorganic salts and organic algicides (such as copper salts, $CuSO_4$, NaOCl, and phthalate esters),[30-31] a water-insoluble agent can be applied directly to the bloom area and can be wholly recovered from the targeted area without being released into the environment, thus not damaging non-target organisms.

Preliminary studies revealed that $(DHS)Bi_2I_8$ and $(DHT)(H_3O)_2Bi_4I_{16}\cdot 2(H_2O)$ suppressed *K. brevis* growth at concentrations as low as 10 mg/L. Such inhibition was found at significantly lower concentrations of materials than the effective inhibitory concentrations of previously reported bacterial strains (1 mg/mL). Toxicity evaluation indicated selectivity towards *K. brevis*, as inhibition was not seen against other marine algae strains such as *Nannochloropsis oculata (N. oculata)* and *Tetraselmis suecica* (*T. suecica*) at similar concentrations, demonstrating the non-toxic impact of PMHS on non-target, beneficial green algae in the marine ecosystem.

This work showcases the ubiquitous nature of our synthetic methodology for acquiring potentially permanent water-stable MHS, coupled with tunable porosity and optoelectronic properties. Moreover, we unveil the structural versatility of PMHS materials and their significant potential for intricate applications, such as HAB mitigation. It is pointed out that this is the first time a MHS material has been evaluated for this purpose.

EXPERIMENTAL SECTION

Many of the methods utilized here are also reported in this reference.[17]

Starting materials.

All starting materials for synthesis were purchased commercially and were used without further purification. Bismuth(III) oxide, 98+%, was purchased from Acros Organics, Hydriodic acid 57 wt. % in H_2O, distilled, stabilized, 99.95% purchased from Sigma-Aldrich, 1-chloro-2-(2-(2-(2-chloroethoxy)ethoxy)ethoxy)ethane (98%) and 2,2'-(oxybis(2,1-ethanediyloxy))bis[ethanamine] (98%) were purchased from Aaron chemicals. Sodium iodide 99.5%, potassium carbonate 99%, sodium chloride 99%, sodium thiosulfate 98%, acetone 99.5%, acetonitrile 99.9%, methanol >95%, ethyl acetate 99.5% and dimethyl sulfoxide (DMSO) 99.9% were provided by Fisher Chemical. THF 99.9% was purchased from Thermo Scientific. For the stability experiments, the following amounts of materials and solvents were utilized. Water: 200mg in 4mL, salt water: 150mg in 8mL, acid: 150mg in 4mL.

XRD measurements.

Single-crystal X-ray diffraction

X-ray diffraction data were measured on a Bruker D8 Venture PHOTON II CMOS diffractometer equipped with a Cu Kα INCOATEC ImuS micro-focus source (λ = 1.54178 Å) equipped with a cryostream 800 system (Oxford Cryosystems) for temperature regulation. Indexing was performed using APEX4 (Difference Vectors method).[32] Data integration and reduction were performed using SaintPlus.[33] Absorption correction was performed by a multi-scan method implemented in SADABS.[34] Space group was determined using XPREP implemented in APEX3. Structure was solved using SHELXT[35] and refined using SHELXL-2018/3 (full-matrix least-squares on F2)[36] through OLEX2 interface program.[37] Ellipsoid plot was done with Platon.[38] Disordered molecule was refined with restraints. All hydrogen atoms were located geometrically and were refined using a riding model.

Bond angle variance (σ^2) parameters were determined using the following formula[39]:

$\sigma^2=\frac{1}{11}\sum_{i=1}^{12}(\theta_i-90°)^2$, ($\theta_i$ are the 12 I−Bi−I bond angles within an octahedron).

Powder X-ray diffraction

Powder X-ray diffraction patterns were collected on a Bruker D8 Advance Diffractometer with a Lynxeye detector using CuKα radiation. X-ray source operated at 40kV/40mA and Ni filter was used to suppress Kbeta radiation. 2.5 deg primary and secondary Soller slits were used to suppress axial divergence. Diffraction patterns were recorded from 2 to 60 2θ in variable slits mode and with knife edge installed. A typical scan rate was 20 sec/step with a step size of 0.02 deg.

Optical Spectroscopy

Optical diffuse-reflectance measurements were performed at room temperature using a Cary 5000 UV-Vis-NIR Spectrophotometer, coupled with an integrating sphere, from 200 to 2500 nm. $BaSO_4$ was used as a non-absorbing reflectance reference. The generated reflectance-versus-wavelength data were used to estimate the band gap of the material by converting reflectance to absorbance data according to the Kubelka−Munk equation: $\alpha/S = (1 - R)^2/2R$, where R is the reflectance and α and S are the absorption and scattering coefficients, respectively.[40]

TGA-DSC measurements

Thermogravimetric Analysis (TGA) measurements were performed on a TA Instruments Q50 Thermogravimetric Analyzer. An amount of ~12 mg of sample was placed inside an Alumina Pan and heated up to 700 °C under N_2 flow with a heating rate of 5 °C/min. Differential Scanning Calorimetry (DSC) measurements were performed on a TA Instruments Q20 Differential Scanning Calorimeter. A sample of 3 mg was placed inside an aluminum pan and heated up to 250 °C under N_2 flow with a heating rate of 5 C/min.

SEM/EDS measurements

The SEM/EDS was performed with a Hitachi SU70 SEM using an IXRF SDD EDS system. The samples were prepared by pressing the powder on to a substrate of carbon adhesive tape and tilting the sample to 30 degrees. The electron beam energy was set to 5 KeV for SEM and 16 KeV for EDS.

^{1}H-NMR and ^{13}C-NMR

The ^{1}H and ^{13}C NMR experiments were recorded using a Bruker AVANCE III HD 600 M*Hz* spectrometer. Data are reported as follows: chemical shifts in ppm, multiplicity (s= singlet, br= broad, t= triplet, multiplet = m, *J* = coupling constant represented in *Hz*.

LC-MS studies

LC-MS studies were performed on an Agilent LC-MS SQ 6120 equipped with an Agilent 1100HPLC diode array detector (DAD) using electrospray (ESI) atmospheric pressure chemical ionization (APCI ± ve).

Gas sorption measurements

Gas sorption measurements for N_2 (99.999%) and CO_2 (99.999%) were recorded at 77 K and 195 K respectively up to 1 bar, using a state-of-the-art, high precision BELSORP-MAX X from Microtrac MRB, equipped with four (4) analysis stations and a detachable thermostatic bath for accurate measurements. For the aforementioned measurements the desired cryogenic temperature was achieved using a bath of liquid nitrogen (LN_2, 77 K, N_2) and a mixture of acetone/dry ice (195 K, CO_2) in a cryogenic dewar as a coolant. The bright red powder sample was placed in a 9 mm pre-weighted quartz cell and then it was activated at 180 ^{o}C (5 °C/min) for 12 hours, under vacuum. After the activation process the cell was re-weighted to measure the exact mass (0.1555 g) of the sample and then it was placed at the analysis station.

Vapor sorption measurements

Vapor sorption isotherms for H_2O were recorded at 298 K up to 1 bar, using the same apparatus. The desired temperature was achieved with the use of the detachable thermostatic bath. The material was re-activated following the procedure described above. Prior to measurements, the vapor was degassed to remove any dissolved gases following a standard protocol. For comparison purposes, all isotherms are presented as the amount adsorbed as a function of the relative pressure, p/p_0, where p_0 is the saturation pressure of the vapor at the measurement temperature.

DFT Studies

We carried out density functional theory (DFT) calculations as implemented in the Quantum ESPRESSO package.[41-42] For the reaction energies, the Kohn-Sham wave-functions and energies are calculated with the GGA-PBE[43-44] for electron exchange and correlation, using a plane-wave basis, with energy and charge density cutoffs of 50 and 400 Ry, respectively. The Grimme dispersion correction DFT-D3,[45-46] was used to account for the dispersion corrections. Ultrasoft pseudopotentials are used to describe the core-valence interactions.[47] The structural relaxation is performed until the force on each atom is smaller than 0.01 eV/Å. For the geometry optimization, a *k*-point sampling of 3x3x3 was used for the Brillouin zone integration and a 5x5x5 k-mesh for the electronic structure analysis following the Monkhorst-Pack scheme.[48] The formation energies were calculated as the difference between the total energies of products (systems) and the reactants (precursors):

E_f = E(products) -ΣE(reactants), for the two systems

$(DHT)I_2 + 4BiI_3 + 2HI + 4H_2O \rightarrow (DHT)(H_3O)_2{\cdot}Bi_4I_{16}{\cdot}2(H_2O)$

$(DHT)I_2 + 2BiI_3 + 2H_2O \rightarrow (DHT)Bi_2I_8 \cdot 2(H_2O)$

The dielectric functions of the two systems were calculated using epsilon.x included in the Quantum ESPRESSO package within the independent particle approximation, which neglects local field effects. A Gaussian broadening of 0.15 was applied and both the real and imaginary parts were subsequently used to derive the absorption coefficient.

Algae Growth and Inhibition Studies

Karenia brevis MK-620 (henceforth *K. brevis*) was obtained from the W.R. Mote Aquaculture Park and maintained in filtered seawater media for 24 hours to determine the reduction of cultured *K. brevis* cells. Flask experiments were conducted in the laboratory under ambient fluorescent light. The experimental cultures of *K. brevis* cells were prepared in 1-L flasks containing filtered seawater growth medium, which was inoculated with an exponentially growing culture at an initial concentration of 10^6 cells/L. Each flask was inoculated with the respective concentration of materials and cell counts were confirmed via microscopic enumeration at 100X magnification using a direct microscope. All experiments were run in triplicate and cell counts were confirmed 24 hours after the introduction of the materials to determine the inhibitory effects of the PMHS.

Nannochloropsis oculata CCMP 525 (henceforth *N. oculata*) was procured from the National Center for Marine Algae and Microbiota (NCMA) (Bigelow laboratory for Ocean Sciences, Maine, USA). *Tetraselmis suecica* UTEX LB 2286 (henceforth *T. suecica*) was purchased from the culture collection of algae at the University of Texas (Austin, USA). *N. oculata* and *T. suecica* were maintained in macronutrient modified F/2 (Phyto Technology Laboratories, USA) marine medium. The pH of all the media was set at 7.5 using a pH meter (Orion 3 Star, Thermo Fisher, USA). For inoculum preparation, the algal strains were cultivated at an optical density of 0.2 at 750 nm ($O.D._{750nm}$) at concentrations of 10 mg/L and 30 mg/L alongside negative controls (no addition of any materials) of the $(DHS)Bi_2I_8$ and the $(DHT)(H_3O)_2Bi_4I_{16} \cdot 2(H_2O)$ materials in the respective media using 125-mL Erlenmeyer flasks with a working volume of 50 mL under continuous white light with an intensity of 100 µmol/m^2s in an incubator shaker (Excella E24, New Brunswick Scientific, Eppendorf, Germany) at 150 rpm at 25 °C for 7 days. OD_{750nm} values were recorded every 24 hours to monitor algal growth after exposure to the materials.

Type I ROS Studies

UV- Vis measurements were performed at room temperature using a Shimadzu UV-1900i UV-Vis Spectrophotometer. 10 mg of sample were sonicated in 1 mL of deionized water until a suspension was formed. 40 mg of N,N,N',N'-tetramethyl-p-phenylenediamine (TMPD) were dissolved in 1 mL of deionized water. 30 µL of the material solution were added to 3 mL of DI water, fresh F/2 media, and spent F/2 media before 30 µL of the TMPD solution was added. Measurements were recorded before and after irradiation with a 50W IP66 LED Floodlight, noting times of color changes that indicate the presence of Type I ROS.

Type II ROS Studies

UV-Vis measurements were performed at room temperature using a Shimadzu UV-1900i UV-Vis Spectrophotometer. 10 mg of sample were sonicated in 1 mL of deionized water until a suspension was formed. A 1 mmol of 9,10-anthracenediyl-

bis(methylene)dimalonic acid (ABDA) was prepared in DMSO. 30 µL of the material solution were added to 3 mL of DI water before 30 µL of the ABDA solution was added. The sample was then irradiated by a 50W IP66 LED Floodlight for 30 minutes. Measurements were recorded over ten-minute intervals, noting the degradation of ABDA and the presence of Type II ROS.

RESULTS AND DISCUSSION

Synthetic aspects and structural characterization

In order to study the effect of porosity on the water stability and optoelectronic properties of PMHS compounds, we targeted the synthesis of PMHS materials featuring the same inorganic part composition and structure dimensionality but with tunable pore size. Toward this goal, we designed and synthesized a custom-made molecular cage,[49] namely [3.3.3] cryptand (DHT), expanding the cavity of previously reported [2.2.2] cryptand (DHS) from 4.3 to 6.2 Å, distance measured among the protons of the ammonium groups (-N-H$^{\cdots}$H-N-), van der Waals radii excluded.

The reaction between Bi_2O_3 and the DHT linker in a hot HI solution gave rise to $(DHT)(H_3O)_2Bi_4I_{16}{\cdot}2(H_2O)$ as dark orange microcrystals (Figure S6). Single-crystal X-ray diffraction (XRD) studies uncovered a 0D structure that crystallizes in the orthorhombic space group *Pnn*2 (Figure 1 and Table 1). The uniform composition and crystallinity of the as made material was confirmed using in-house powder X-ray diffraction, as the experimental and calculated patterns from single-crystal XRD studies are identical (Figure 2), while energy-dispersive X-ray spectroscopy (EDS) studies validated the $(DHT)(H_3O)_2Bi_4I_{16}{\cdot}2(H_2O)$ formula, revealing a Bi:I ratio of 1:4.3 (Figure S7). The inorganic part of the structure is a tetranuclear $[Bi_4I_{16}]^{4-}$ cluster featuring three crystallographically independent Bi(III) atoms and eight I atoms. Due to the presence of two glide planes perpendicular to *a* and *b* crystallographic axes and 2-fold rotation parallel to *c-axis*, asymmetric units of three independent Bi(III) atoms generate isolated Bi(III) iodide tetramers consisting of edge-sharing $[BiI_6]^{3-}$ octahedra along the *c-axis* (Figure 1c). The inorganic anionic clusters are separated and charge-balanced by the DHT ligands and two H_3O^+. One H_3O^+ resides in the cage, and the other one in the interstitial space. The structure is completed by two crystalline H_2O molecules lying in the interstitial space as well. Adjacent tetramers lie at a distance of 4.1 Å and 7.1 Å along the *c* and *b* axes, while corresponding clusters are eclipsed.

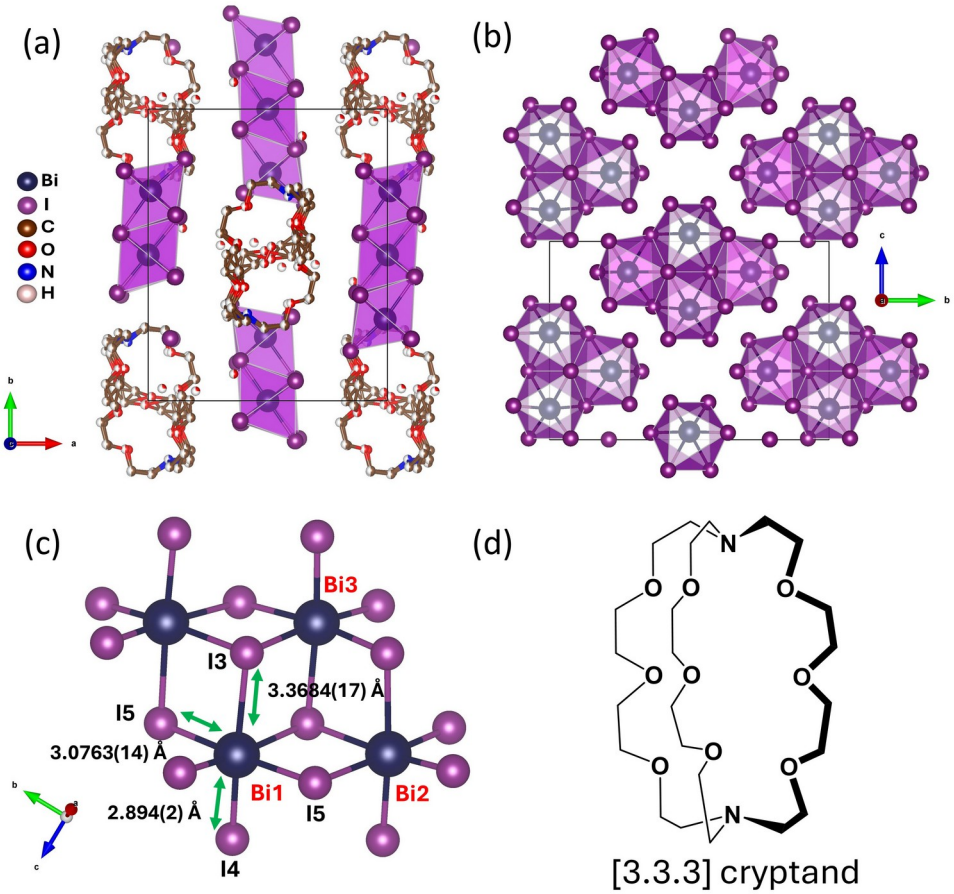

Figure 1. (a) The unit cell contents of the crystal structure of $(DHT)(H_3O)_2Bi_4I_{16}\cdot 2(H_2O)$ viewing along the *c*-axis. (b) Part of the crystal structure along the *a*-axis showcasing the packing of the inorganic clusters. (c) The structure of the inorganic $[Bi_4I_{16}]^{4-}$ tetramer showing the octahedral connectivity and representative Bi-I bond lengths. (d) Molecular representation of the [3.3.3] cryptand (DHT) molecular cage.

Underlying Bi-I bond lengths span from 2.894(2) Å to 2.9528(12) Å and from 3.0763(14) Å to 3.3684(17) Å, for the non-bridging and bridging iodide atoms, respectively (Table S3). These values align well with those of other iodobismuthate(III) systems,[50-51] such as $(TMPZ)BiI_5$ (TMPZ = 1,1,4,4-tetramethylpiperazine) and $(S\text{-}MeTMPZ)BiI_5$ (S-MeTMPZ = (S)-1,1,2,4,4-pentam-ethylpiperazinium.[52] The edge-sharing octahedra feature a slight distortion that is manifested in the bond angle variance (σ^2) values of 12.4 deg.^{2}, 13.7 deg.^{2} and 17.7 deg.^{2} for each crystallographically independent Bi(III) respectively (see experimental section for corresponding formulas).

Table 1. Crystal and structure refinement data for $(DHT)(H_3O)_2Bi_4I_{16}\cdot 2(H_2O)$ and $(DHT)Bi_2I_8\cdot 2(H_2O)$ at 298 K and 296 K respectively.

	$(DHT)(H_3O)_2Bi_4I_{16}\cdot 2(H_2O)$	$(DHT)Bi_2I_8\cdot 2(H_2O)$
Crystal system	orthorhombic	triclinic
Space group	*P n n* 2	*P*-1
	a = 15.1457(3) Å, α = 90°	a = 12.6298(6) Å, α = 110.107(2)°

This distortion arises from the bond angle variation from an ideal octahedron, such that I-Bi-I angles range from 82.27(5)° to 177.42(7)° for the cis and trans arrangements, respectively (Table S4). Comparable octahedral distortion values have been reported before with other $[Bi_4I_{16}]^{4-}$ tetramer-based compounds, such as $(AmV_2)Bi_4I_{16}$ that exhibit σ^2 values of 29.7 deg.^{2} and 10.3 deg.^{2}.[53]

Compared with $(DHS)Bi_2I_8$ structure, it was found that the inorganic clusters are the same. Specifically, Bi-I bond lengths and I-Bi-I angles closely match the two materials, albeit $(DHT)(H_3O)_2Bi_4I_{16}\cdot 2(H_2O)$ features a lower level of distortion for the inorganic part, based on recorded σ^2 values. Determined values range from 12.4 deg.^{2} and 13.7 deg.^{2} to 17.7 deg.^{2} for the $(DHT)(H_3O)_2Bi_4I_{16}\cdot 2(H_2O)$ and from 37.65 to 18.34 deg^2 for the $(DHS)Bi_2I_8$ compound, respectively.

The organic counter-cations are eclipsed along all crystallographic axes, lying at a distance of ~5.7 Å and ~9.5 Å along the *c* and *a* axes, respectively, revealing a brick wall packing motif (Figure 1a). DHT molecules are disordered over two positions across a 2-fold axis. This packing configuration is distinctly different from that observed for the $(DHS)Bi_2I_8$ material, where the DHS molecules feature a hexagonal arrangement motif.

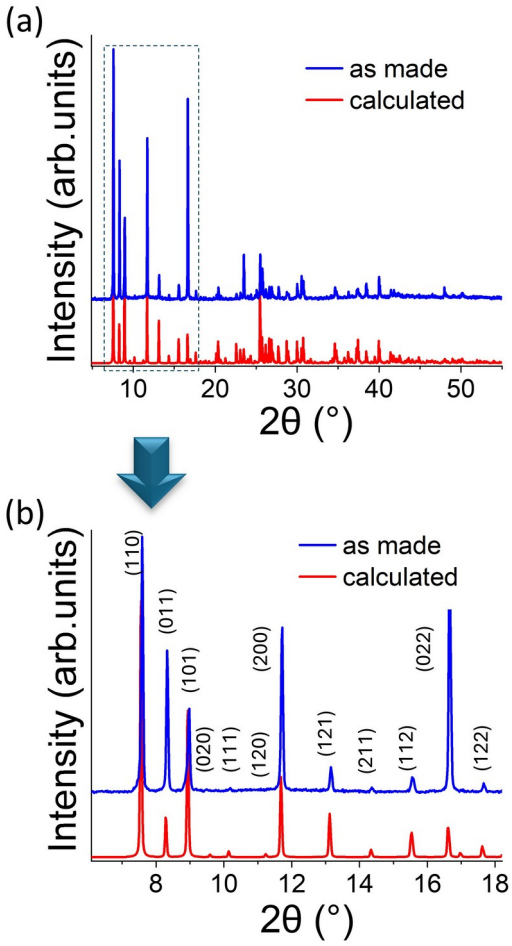

Figure 2. (a) Comparison of the PXRD patterns for the as-made (DHT) $(H_3O)_2Bi_4I_{16}{\cdot}2(H_2O)$ crystals to the calculated pattern based on the solved single crystal structure. (b) Zoom into the highlighted area of the PXRD patterns from 6° to 18° 2θ, verifying the high crystallinity and phase purity of the as-made sample.

To investigate the thermal stability of the corresponding material, thermogravimetric (TGA) analysis and differential scanning calorimetry (DSC) measurements were performed. TGA plot reveals that the material loses its crystalline H_2O and H_3O^+ gradually up to 170 °C, which is confirmed by the DSC measurements that show two endothermic peaks at ~120 °C and ~170 °C (Figure S8). The structure maintains its thermal integrity up to 245 °C, at which point a sharp decline in the corresponding sample mass is observed.[54] Two degradation steps were recorded at ~250 °C and ~320 °C (Figure S8a). We assign the first weight loss, accounting for ~23% mass loss, to the decomposition of the organic part of the structure and HI, and the second step, being approximately 65%, to the sublimation of BiI_3, correlating well with other literature reports.[55,50]

Water stability behavior

Immersion of fresh as-made crystals in liquid water for 24 months revealed a SCSC transformation, giving rise to (DHT)Bi_2I_8·2(H_2O), a 0D material crystallizing in the triclinic space group *P*-1 (Figure 3 and Table 1). The structure features the same inorganic part as the parent (DHT)(H_3O)$_2Bi_4I_{16}$·2(H_2O) (Figure S9a). There are two crystallographically independent Bi atoms and eight I atoms that constitute the four octahedra of the tetramers. Corresponding octahedra feature a slightly larger degree of distortion, as compared to the (DHT)(H_3O)$_2Bi_4I_{16}$·2(H_2O), deriving from determined σ^2 values of 11.9 deg.^{2} and 23.8 deg.^{2} However, the configuration of the organic molecules is different. There is no disorder, and there are no H_3O^+ in the crystal structure; rather, there are two crystalline H_2O molecules in the DHT cavities (Figures 3c and S9c,d). The aforementioned H_2O molecules are stabilized by multiple strong hydrogen bonds spanning from 1.8 Å to 2.1 Å, deriving from interactions with the ammonium (-NH_3^+) and ether (-CH_2-O-CH_2-) groups of the ligand. Comparison of the calculated and experimental PXRD patterns reveals that the (DHT)(H_3O)$_2Bi_4I_{16}$·2(H_2O) has completely transformed into a major (DHT)Bi_2I_8·2(H_2O) phase and another secondary phase, which was not possible to be identified by means of single crystal XRD studies (Figures S10).

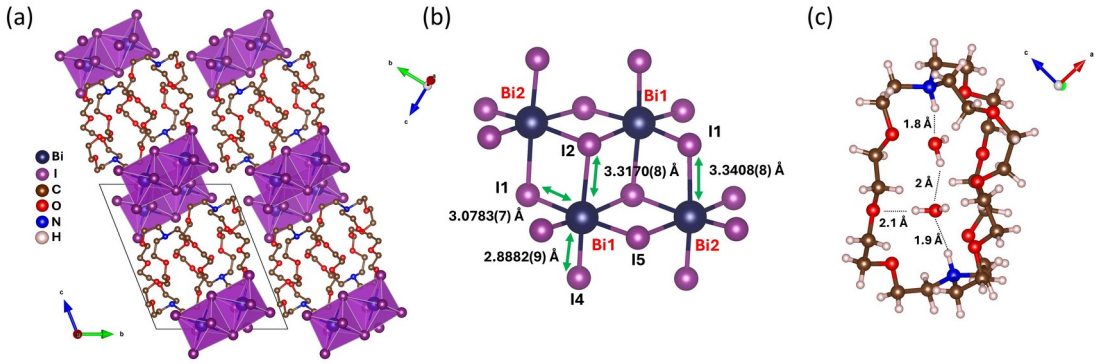

Figure 3. (a) The unit cell contents of the crystal structure of (DHT)Bi_2I_8·2(H_2O) viewing along the *a*-axis. (b) The structure of the inorganic $[Bi_4I_{16}]^{4-}$ tetramer showing the octahedral connectivity and representative Bi-I bond lengths. (c) A molecular cage filled with two H_2O molecules, stabilized through multiple strong hydrogen bonds.

It should be noted that SCSC transformations upon water treatment have been recorded before for MHS materials.[56-57-58] Zhang et al., reported a reversible moisture-induced dimensional transformation for the 1D $PDABiI_5$ (PDA = 1,3-propane diammonium) which converted into the 0D dimeric (PDA)$_2Bi_2I_{10}$·2H_2O,[59] while Kandel

et al., observed that $Cs_3BiBr_6 \cdot 3DMSO$ underwent an SCSC transition yielding the Cs_3BiBr_6 phase upon exposure to MeOH vapors.[60]

Notably, as made single crystals remained in their mother solution (conc. HI) for at least four months without any structural degradation, demonstrating the robustness of the crystal structure under strongly acidic conditions (Figure S11).

Despite the observed phase transition, it is safe to claim that the use of the DHT molecules as structure-directing agents and counter-cations did indeed give rise to a water-stable material with performance similar to $(DHS)Bi_2I_8$ (20 months in water), affirming the general applicability of our synthetic strategy for the acquisition of porous and water-stable metal halide semiconductors.

Gas and vapor sorption studies

N_2 and CO_2 sorption isotherms recorded at 77 K and 195 K, respectively, in a previously activated $(DHT)(H_3O)_2Bi_4I_{16} \cdot 2(H_2O)$ at 180 °C under vacuum, showed no gas uptake (Figure 4a). Meanwhile, due to the water-stable nature of the material, we performed H_2O vapor sorption studies at 298 K, revealing a reversible sorption (closed loop) (Figure 4b). At 298 K, an uptake of 0.67 mmol g^{-1} at 0.8 p/p_0 was recorded, which is close to the calculated value of 0.6 mmol g^{-1}, assuming two H_2O molecules inside the cavity of DHT, as it was elucidated from the XRD and DFT studies (Figure 4b). The slight hysteresis observed during desorption may be attributed to the magnitude of hydrogen bonding between the adsorbates and the framework, supported further by their narrow confinement. Similar behavior has been observed before for microporous Metal Organic Frameworks (MOFs), such as DUT-69.[61] Nevertheless, the overall sorption process remains fully reversible, indicating the interactions of H_2O within the material are relatively mild (physisorption). It is noted that the points of the isotherms close to 0.99 p/p_0 suggest condensation associated with interparticle meso/macro-porosity due to the polycrystalline nature of the sample.

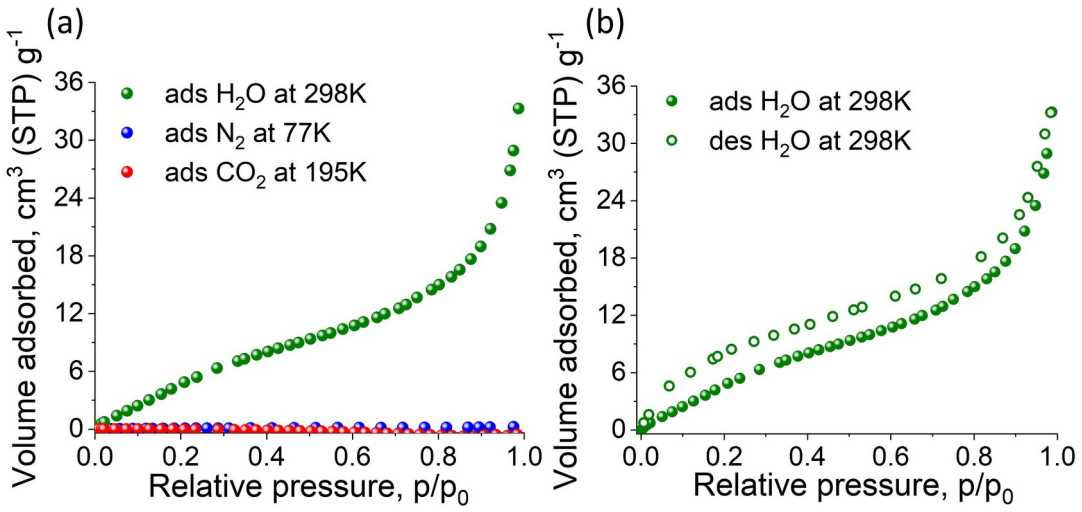

Figure 4. (a) N_2, CO_2, and H_2O isotherms at 77 K, 195 K, and 298 K respectively. (b) H_2O adsorption and desorption isotherms recorded at 298K up to 1bar, the reversible character of the isotherm is indicative of physisorption of the vapor molecules in the adsorbent.

The results demonstrate that the available space created by DHT cages is accessible by H_2O in the 0D (DHT)Bi_2I_8 solid, featuring a very similar isotherm to the 2D $(DHS)_2Pb_5Br_{14}$ material rather than the 0D (DHS)Bi_2I_8. Based on the shape of the isotherm, which shows a gradual increase in H_2O uptake (no knee) associated with slow adsorption kinetics, we hypothesize that, despite DHT featuring a larger cavity than DHS, the higher flexibility of the former cage might be responsible for the slower vapor diffusion. Upon crystalline H_2O and H_3O^+ removal after activation, the cage might twist to accommodate the lost space, dwindling its pore cavity, thus slowing down incoming H_2O molecules.

DFT studies

In order to shed light on the thermodynamic stability of (DHT)$(H_3O)_2Bi_4I_{16}\cdot 2(H_2O)$ over (DHT)$Bi_2I_8\cdot 2(H_2O)$, we performed DFT calculations on their formation energies. The calculated values were -2.84 eV and -2.91 eV per formula unit, respectively, indicating that (DHT)$Bi_2I_8\cdot 2(H_2O)$ is thermodynamically more stable by approximately 70 meV. The small energy difference points out (DHT)$(H_3O)_2Bi_4I_{16}\cdot 2(H_2O)$ as a metastable phase. The fact that this transition took about 24 months likely depicts not only the modest thermodynamic driving force favoring (DHT)$Bi_2I_8\cdot 2(H_2O)$, but also a significant kinetic barrier associated with structural reorganization.

Figure 5 shows the electronic band structure evolution with H_2O loading for $(DHT)(H_3O)_2Bi_4I_{16}\cdot 2(H_2O)$ and $(DHT)Bi_2I_8\cdot 2(H_2O)$, respectively. Both compounds exhibit direct band gaps at the Γ and V high-symmetry points of their corresponding Brillouin zones, with values of 1.15 eV and 1.52 eV, respectively, without the presence of H_2O in the DHT. Upon water loading (two H_2O molecules per DHT), the band gap of $(DHT)(H_3O)_2Bi_4I_{16}\cdot 2(H_2O)$ increases to 1.36 eV, whereas the band gap of $(DHT)Bi_2I_8\cdot 2(H_2O)$ marginally decreases to 1.51 eV. This trend in the corresponding bandgap values matches well with the difference in distortion between the two materials, with $(DHT)Bi_2I_8\cdot 2(H_2O)$ featuring a slightly higher distortion compared to $(DHT)(H_3O)_2Bi_4I_{16}\cdot 2(H_2O)$ (see water stability behavior section above). It is pointed out that underlying structural distortions typically dominate the extent of metal-halogen (M-X) orbital overlap and the optoelectronic properties in hybrid metal-halide semiconductors.[62]

We note that the calculated band gap values, obtained using DFT-PBE with spin-orbit coupling (SOC), are underestimated compared to the experimentally measured band gaps. These variations in the band gaps of the two systems with H_2O loading are likely due to changes in the crystal structures that occur when H_2O is incorporated into the DHT cage. Specifically, for $(DHT)(H_3O)_2Bi_4I_{16}\cdot 2(H_2O)$, the lattice vectors *a* and *c* increase by 2.3% and 1.6%, respectively, whereas, *b* decreases by 0.4 %. In the case of $(DHT)Bi_2I_8\cdot 2(H_2O)$ all the lattice vectors, *a*, *b*, and *c* increases by 1.4 %, 0.5%, and 0.2%, respectively. We also note that the bands are more disperse in the case of $(DHT)Bi_2I_8\cdot 2(H_2O)$. Evidently, SOC has a greater influence in the electronic structure of $(DHT)(H_3O)_2Bi_4I_{16}\cdot 2(H_2O)$, since the degeneracy of the bands is lifted, leading to a discernible Rashba-type band splitting, in particular near the CBM, which arises from the non-centrosymmetry of the system. In contrast, the triclinic $(DHT)Bi_2I_8\cdot 2(H_2O)$ system exhibits no splitting, with its band structure remaining unchanged upon the inclusion of SOC.

Examining closely the density of states (Figure S12) we observe that the valence band region near the VBM in both materials is mainly dominated by the I and O atoms, whereas the conduction band region near the CBM is dominated by the Bi and I, similar to other metal halide semiconductors. In particular, around the VBM, the states feature a contribution mainly from the 5p orbitals of the I atoms and the 2p orbitals of the O atoms. A small contribution from the carbon 2p orbital and the hydrogen 1s orbitals is also noticeable. The CBM is mainly composed of the 6p orbitals of Bi atoms and the 5p

of the I atoms. Therefore, the states of the O species deriving from the organic part of the structure can potentially contribute to the electrical and optical properties of the materials.

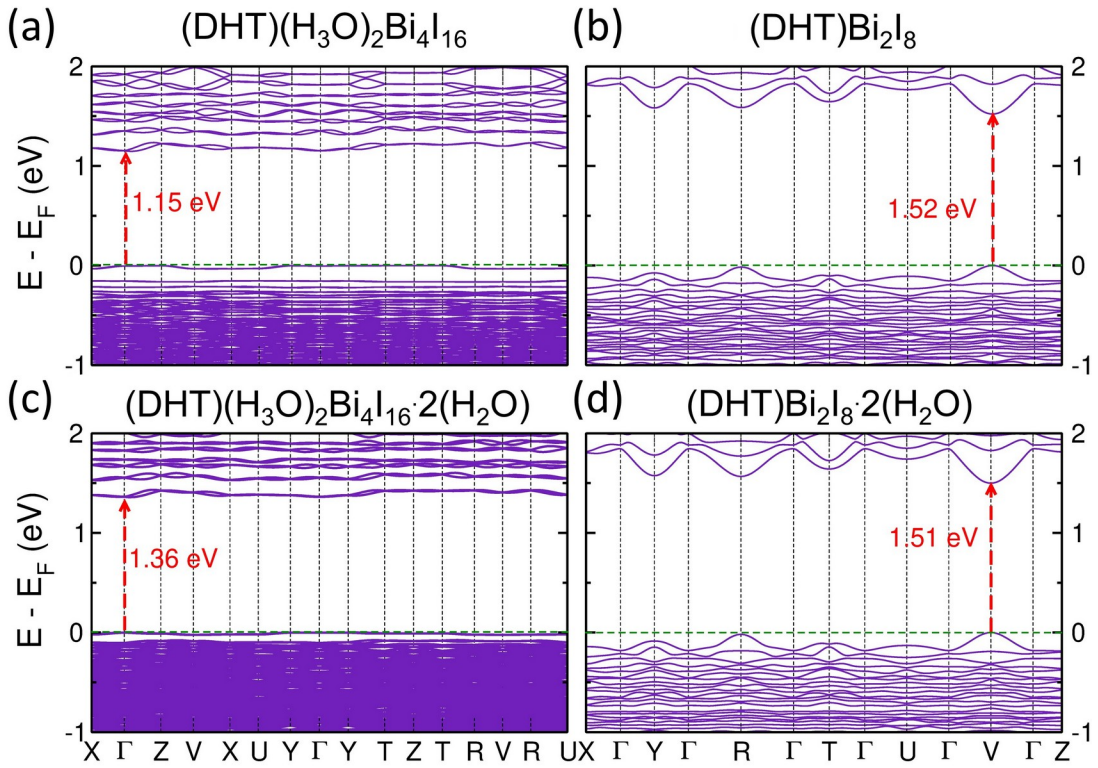

Figure 5. Band structure evolution of $(DHT)(H_3O)_2Bi_4I_{16}\cdot 2(H_2O)$ and $(DHT)Bi_2I_8\cdot 2(H_2O)$ with water loading. (a) and (b) no water loading, (c) and (d) two H_2O molecules per one DHT cage.

The calculated real and imaginary parts of the dielectric function are shown in Figure S13. Both $(DHT)(H_3O)_2Bi_4I_{16}$ and $(DHT)Bi_2I_8$ exhibit similar static dielectric constants of approximately 4 in the limit of zero photon energy, indicating comparable low-frequency polarization response. However, their frequency-dependent dielectric functions differ noticeably. As the energy increases, the real part (Re(ε)) shows the highest peak intensity at 2.1 and 2.2 for $(DHT)(H_3O)_2Bi_4I_{16}$ and $(DHT)Bi_2I_8$, respectively. The imaginary part of the dielectric function for $(DHT)(H_3O)_2Bi_4I_{16}$ shows a gradual onset starting around 1.5 eV, followed by a sharp and pronounced peak at higher energy. In contrast, $(DHT)Bi_2I_8$ exhibits an immediate and steep rise at slightly higher energy, indicating a more abrupt absorption onset and suggesting a slightly higher optical band gap relative to the former. These differences imply that (DHT)

$(H_3O)_2Bi_4I_{16}$ supports more complex electronic transitions, likely influenced by its non-centrosymmetric orthorhombic structure and the presence of spin–orbit coupling (SOC), which lifts band degeneracy and introduces Rashba-type splitting near the conduction band minimum, along with non-dispersive flat bands. In contrast, the centrosymmetric triclinic (DHT)Bi_2I_8 displays a simpler dielectric response.

Optical properties

Utilization of the Kubelka-Munk equation (see experimental section) allowed the determination of the optical absorbance of the fresh and water-treated materials from UV-vis diffuse reflectance studies (Figure 6). Notably, (DHT)$(H_3O)_2Bi_4I_{16}\cdot 2(H_2O)$ features a sharp absorption edge at 2.04 eV.

To evaluate the material's photoluminescence emission, (DHT) $(H_3O)_2Bi_4I_{16}\cdot 2(H_2O)$, a 475 nm monochromatic light was utilized, offering enough energy to excite the carriers across the bandgap. We observed broad, band-edge light emission centered at 608 nm (2.04 eV) with a full width at half maximum (FWHM) of 119 nm (0.38 eV) (Figure 6a). Photoluminescence excitation (PLE) measurements demonstrated no change in the PL peak profile for the material, centered at 608 nm in the examined excitation region from 405 nm to 485 nm (Figure 6b). The measured average decay lifetime at RT is 0.33 ns determined by time-correlated single-photon counting (TCSPC) spectroscopy measurements. Through deconvolution with the instrument response function (IRF), multiexponential fitting of the emission decay curve shows two components with decay constants of 0.07 and 3.4 ns (Figure S10). This PL emission performance is the same as in the case of the (DHS)Bi_2I_8 material, which features the same inorganic part ($[Bi_4I_{16}]^{4-}$) and structure dimensionality (0D). Furthermore, the distance between adjacent tetramers is also very similar, 4.1-4.2 Å and 4.1-4.4 Å for the (DHS)Bi_2I_8 and (DHT)$(H_3O)_2Bi_4I_{16}\cdot 2(H_2O)$, respectively along two of the three crystallographic axes. The aforementioned traits validate that the porous nature can be tuned by using larger molecular cages, with

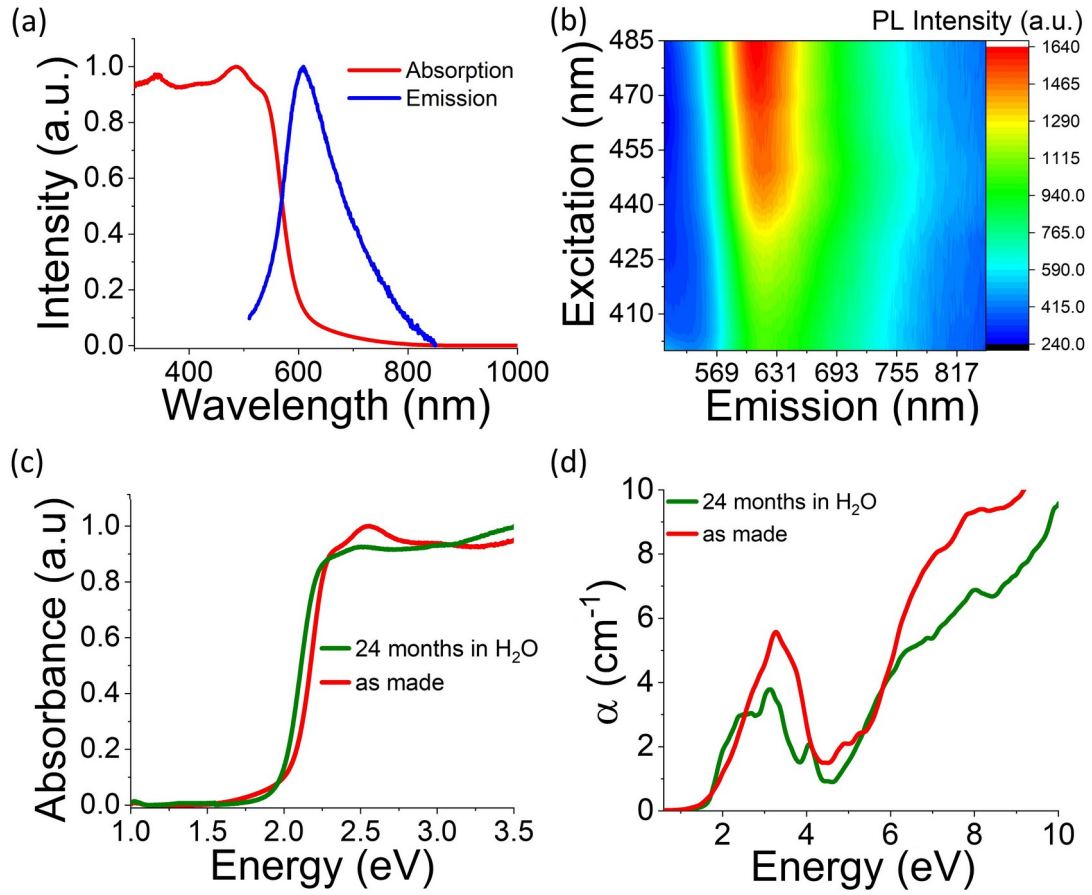

Figure 6. (a) The recorded absorption and emission spectra of (DHT)$(H_3O)_2Bi_4I_{16}{\cdot}2(H_2O)$ compound at RT, (b) PLE spectra map of the pristine material at RT, comparison of the (c) experimental absorbance and (d) calculated absorption coefficient spectra for the fresh sample and the H_2O-treated one, (DHT)$Bi_2I_8{\cdot}2(H_2O)$.

minimum impact on the corresponding optical properties. We point out that band-edge excitonic radiative luminescence in Bi(III) iodides is rare,[63] with few reports only, such as $MA_3Bi_2I_9$.[64]

UV-vis measurements of the water-treated sample (DHT)$Bi_2I_8{\cdot}2(H_2O)$ revealed minuscule changes for the absorption onset compared to the as-made material, which aligns pretty well with the calculated absorption coefficient spectra from DFT studies (Figure 6d). We hypothesize that although from DFT the (DHT)$Bi_2I_8{\cdot}2(H_2O)$ has a larger optical bandgap, what we see from the band structure of (DHT)$(H_3O)_2Bi_4I_{16}{\cdot}2(H_2O)$ relates to a smaller indirect energy transition captured by the tail of the absorbance spectra at ~ 1.6 eV (Figure 6c, red line), while there is another optically active stronger transition that takes place at slightly higher energy than the one observed for (DHT)$Bi_2I_8{\cdot}2(H_2O)$ ((Figure 6c, green line).

Karenia brevis inhibition studies and mechanism of action

K. brevis cell cultures were treated with (DHS)Bi_2I_8 and (DHT) $(H_3O)_2Bi_4I_{16}\cdot 2(H_2O)$ at concentrations of 10mg/L and 30mg/L over the period of 24 hours. The inhibitory activity of the material was assessed via manual cell counts, where it was observed that after 24 h, the inhibition rate was 55 ±3% and 86 ±4.6% at 10 mg/L and 30 mg/L, respectively, for the (DHS)Bi_2I_8 material. A very similar trend was observed for the (DHT)$(H_3O)_2Bi_4I_{16}\cdot 2(H_2O)$ analog, with values of 63 ±4.2% and 85 ±5.7%, respectively (Figure 7). The material performance at these specific concentrations is comparable to other chemical HAB mitigation agents,[30-31] showcasing the immense potential of PMHS against HABs (Table S9). We ascribe this activity to the generation of ROS by the respective PMHS, a common feature of semiconductor materials activated under ambient or UV light conditions.[65] Indeed, recent studies, including those that utilized semiconductor compounds such as TiO_2,[66] validated that ROS can lyse *K. brevis* cells.[27]

The formation of type-I ROS by the (DHS)Bi_2I_8 material was confirmed by the color change of a TMPD (N,N,N',N'-Tetramethyl-p-phenylenediamine) solution from clear to blue after illumination for 131s, resulting from electron transfer between type-I ROS and the dye (Figure S15a). Evaluation of the (DHT)$(H_3O)_2Bi_4I_{16}\cdot 2(H_2O)$ materials indicated a color change after 115s, slightly faster than the DHS analog. We further examined the type-II ROS generation by the degradation of ABDA (9,10-Anthracenediyl-bis(methylene)dimalonic acid), as shown in Figure S15. After 30 minutes of irradiation, 56% and 33% degradation of ADBA was seen for the (DHS)Bi_2I_8 and (DHT)$(H_3O)_2Bi_4I_{16}\cdot 2(H_2O)$ compounds, respectively, indicating the generation of singlet oxygen by these compounds. Therefore, the generation of both type-I and type-II ROS species from PMHS under visible light corroborates our hypothesis for a ROS-based mechanism of action for *K. brevis* inhibition. Importantly, the material maintains its structural integrity after the treatment of crystals in 1% and 3.5% NaCl solution and 1% F2 algae medium for at least 24 hours, as evident by PXRD studies (Figure S16).

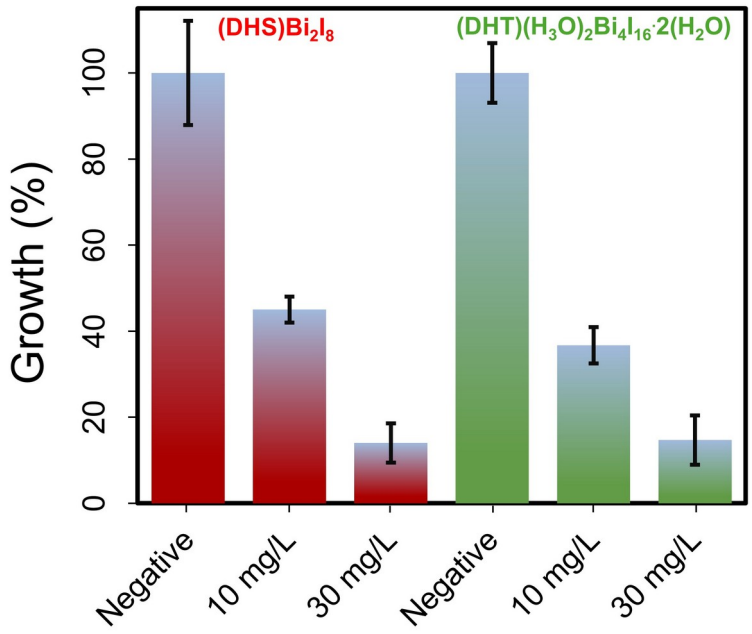

Figure 7. *K. brevis* inhibition by (DHS)Bi_2I_8 and (DHT)$(H_3O)_2Bi_4I_{16}\cdot 2(H_2O)$. The labels "negative" indicate controls, where *K. brevis* was cultivated in the absence of the two compounds.

Toxicity studies

In order to investigate the performance of PMHS against non-target marine organisms, we evaluated the growth of the beneficial marine algae *Nannochloropsis oculata* and *Tetraselmis suecica* in the absence and presence of (DHS)Bi_2I_8 and (DHT)$(H_3O)_2Bi_4I_{16}\cdot 2(H_2O)$. Microalgae, like *N. oculata* and *T. suecica*, are considered to be promising resources for pharmaceuticals, aquaculture, and biofuel production. *N. oculata* is a unicellular, small green algae of the genus *Nannochloropsis* that can be found in marine and freshwater environments. This species plays a crucial role in the global carbon and mineral cycles and is found in oceans worldwide.[67-68] The genus *Tetraselmis* consists of green flagellates that are also present in both marine and freshwater environments.[69] *T. suecica* cells are fast-growing, have an ovoid shape, and a size of approximately 10 micrometers, as shown in Figure 8a.[70] As seen in Figure 8, utilizing the same concentration of PMHS that induced *K. brevis* inhibition had no impact on the growth of these marine algae species as there were negligible changes between the control samples (labeled negative) and the samples inoculated with our materials. In particular, *N. oculata* cells recovered quickly after exposure to both the (DHS)Bi_2I_8 and (DHT)$(H_3O)_2Bi_4I_{16}\cdot 2(H_2O)$ compounds, growing to an average $O.D._{750nm}$ of 0.932, as shown in Figures 8c,d. Furthermore, the tested *T. suecica* cells

demonstrated growth after 24 hours of exposure to concentrations of 10 mg/L and 30 mg/L, respectively, of the (DHS)Bi_2I_8 compound, as shown in Figures 8a,b. Similar results were seen with the (DHT)$(H_3O)_2Bi_4I_{16}\cdot 2(H_2O)$ compound, with negligible variations from the O.D. values in the control samples over 7 days after inoculation, growing to an average $O.D._{750nm}$ of 0.834.

While ROS are highly reactive and non-selective in mechanism, our results show that the examined materials selectively inhibit *K. brevis* without significantly affecting *N. oculata* or *T. suecica*. Both these green algae feature improved antioxidant activity, due to their high concentration of antioxidant compounds, such as carotenoids, chlorophyll α, vitamin E, and tocopherols, which help them resist potential damage from ROS.[71-72-74] Although *K. brevis* has some antioxidant mechanisms,[75] it is much more susceptible to the presence of ROS than the tested species[66, 76].

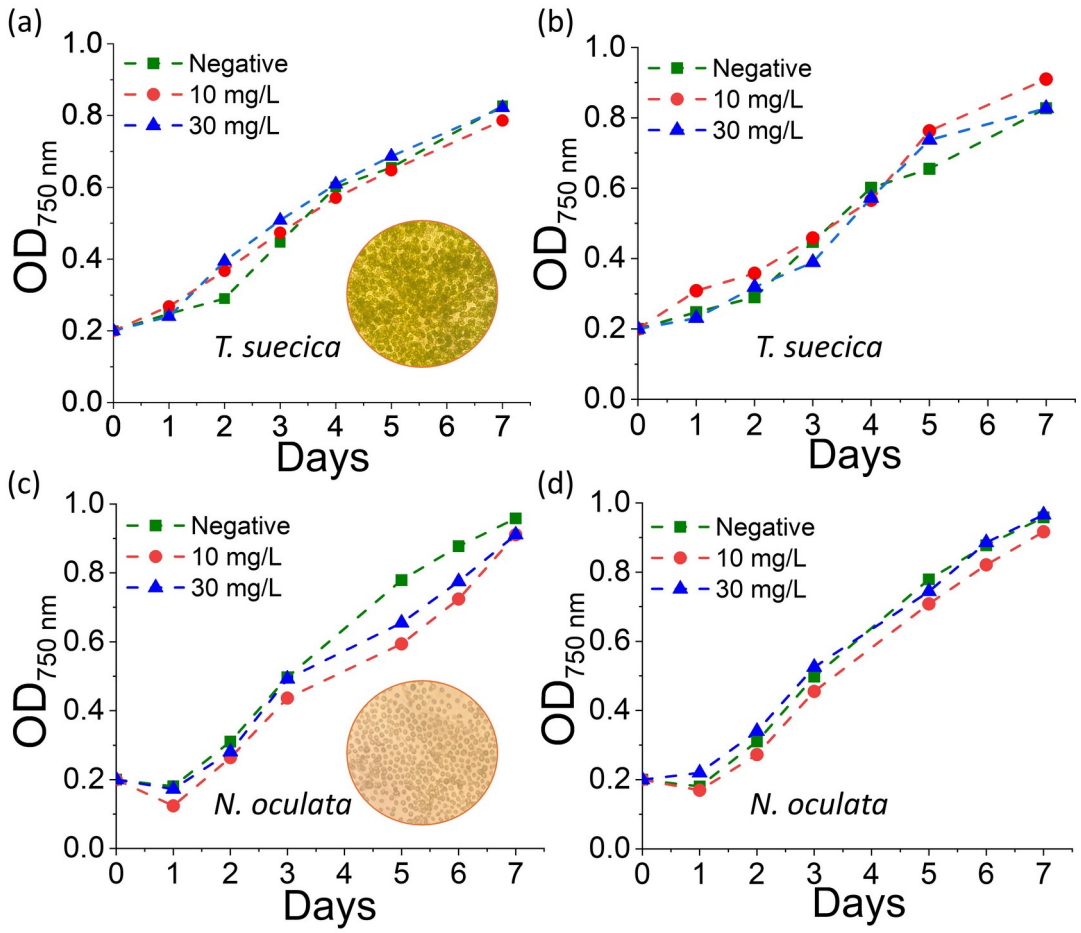

Figure 8. Upper graphs: 7-day growth curves of *T. suecica* after treatment with (a) (DHS)Bi_2I_8 and (b) (DHT)$(H_3O)_2Bi_4I_{16}\cdot 2(H_2O)$. Lower graphs: 7-day growth curves of *N. oculata* after treatment with (c) (DHS)Bi_2I_8 and (d) (DHT)$(H_3O)_2Bi_4I_{16}\cdot 2(H_2O)$. The

inset images present agar plate photos of the two algal species.

CONCLUSIONS

PMHS is a versatile class of semiconductors equipped with record water stability performance, tunable porosity, and optoelectronic properties. However, there is limited understanding of the underlying structure-property relationships, particularly regarding the impact of porosity on each of the aforementioned features. To address this challenge, we aimed to expand the platform of available PMHS materials by utilizing molecular cages with progressively larger cavities as structure-directing agents and counter-cations. Consequently, we designed and synthesized a molecular cage with an elongated cavity, compared to the previously reported DHS molecule, namely DHT, which was utilized for the synthesis of the compound (DHT)$(H_3O)_2Bi_4I_{16}\cdot 2(H_2O)$. The corresponding material is a 0D semiconductor, which features very similar structural characteristics to the previously reported (DHS)Bi_2I_8 material, as both of them are composed of the same inorganic part, isolated $[Bi_4I_{16}]^{4-}$ tetramers. (DHT) $(H_3O)_2Bi_4I_{16}\cdot 2(H_2O)$ has been water-stable for 2 years so far, albeit it exhibits an SCSC transformation to a different 0D phase, namely (DHT)$Bi_2I_8\cdot 2(H_2O)$, featuring the same inorganic part.

Gas and vapor sorption studies demonstrated that it can selectively adsorb and desorb H_2O at RT, while it is impermeable to N_2 and CO_2, showcasing its ultra-microporous nature. beyond its porous nature, the compound is a direct bandgap semiconductor that exhibits broad band-edge emission at room temperature, as evidenced by DFT, UV-vis, and PL studies.

Evidently, the expansion of the molecular cage allowed the fine-tuning of the porous nature of the material (in terms of pore size and water uptake), without imparting the optical properties, and the recorded water stability performance.

Motivated by this combination of attributes, we evaluated (DHT) $(H_3O)_2Bi_4I_{16}\cdot 2(H_2O)$ against *K. brevis*, the alga responsible for HABs. Our studies revealed that (DHT)$(H_3O)_2Bi_4I_{16}\cdot 2(H_2O)$ suppressed *K. brevis* growth at concentrations as low as 10 mg/L. Toxicity evaluations indicated selectivity toward *K. brevis*, as no inhibition was observed against beneficial, non-target marine organisms.

This work elucidates the influence of porosity on both the optoelectronic properties and water stability of PMHS compounds, and underscores their potential for impactful, previously unexplored applications such as HAB mitigation. Notably, the

observed stability suggests that our synthetic methodology to generate porous hybrid semiconductors may lead to permanently water-stable MHS. In turn, this not only addresses currently available material deficiencies but also lays the foundation for the exploitation of these compounds in demanding applications, where water stability, porosity, and semiconduction are interwoven.

ASSOCIATED CONTENT

Supporting Information

Materials and methods, synthetic details, additional supplementary figures and tables about material characterization, X-ray diffraction measurements, photoluminescence measurements, thermogravimetric analysis, NMR, DFT, ROS, EDS, and SEM studies.

Accession Codes

CCDC 2442592-2442593 contain the supplementary crystallographic data for this paper. These data can be obtained free of charge via www.ccdc.cam.ac.uk/data_request/cif,orbyemailingdata_request@ccdc.cam.ac.uk, or by contacting The Cambridge Crystallographic Data Centre, 12 Union Road, Cambridge CB2 1EZ, UK; fax: +44 1223 336033.

AUTHOR INFORMATION

Corresponding Author

spanopoulos@usf.edu

Notes

The authors declare no competing financial interest.

Author contributions

[#]These authors contributed equally.

ACKNOWLEDGMENT

This work was primarily supported by the U.S. Department of Energy, Office of Science, and Office of Basic Energy Sciences under Award Number DE-SC0025485 (material synthesis, characterization, including sorption studies, and structure-property relationships). G.P.P acknowledges support from the Florida Fish and Wildlife Conservation Commission of the State of Florida (managed by the Mote Marine Laboratory) (algae growth and inhibition studies) under the Red Tide Mitigation and Technology Development Initiative. We thank Dr Lukasz Wojtas at the USF's X-ray core facility and the CPAS and NREC core facilities for their help with the characterization of the materials. We also acknowledge the IDRA award by USF for purchasing the sorption instruments utilized in this study and the technical support of the Mote Marine Laboratory. The authors acknowledge the use of the High-End Computing (HEC) facility at Lancaster University and the partly supported fund from Lancaster University's Centre for Global Eco-Innovation.

REFERENCES

1. Tu, Q.; Spanopoulos, I.; Hao, S.; Wolverton, C.; Kanatzidis, M. G.; Shekhawat, G. S.; Dravid, V. P., Out-of-Plane Mechanical Properties of 2D Hybrid Organic–Inorganic Perovskites by Nanoindentation. *ACS Appl. Mater. Interfaces* **2018,** *10* (26), 22167-22173.
2. Chen, Z.; Wang, C.; Xue, J.; Chen, J.; Mao, L.; Liu, H.; Lu, H., Observation of Ferromagnetism in Dilute Magnetic Halide Perovskite Semiconductors. *Nano Lett.* **2024,** *24* (10), 3125-3132.
3. Blancon, J. C.; Stier, A. V.; Tsai, H.; Nie, W.; Stoumpos, C. C.; Traoré, B.; Pedesseau, L.; Kepenekian, M.; Katsutani, F.; Noe, G. T.; Kono, J.; Tretiak, S.; Crooker, S. A.; Katan, C.; Kanatzidis, M. G.; Crochet, J. J.; Even, J.; Mohite, A. D., Scaling law for excitons in 2D perovskite quantum wells. *Nat. Commun.* **2018,** *9* (1), 2254.
4. Mitzi, D. B., Templating and structural engineering in organic–inorganic perovskites. *J. Chem. Soc., Dalton Trans.* **2001,** (1), 1-12.
5. Zhu, H.; Shao, B.; Shen, Z.; You, S.; Yin, J.; Wehbe, N.; Wang, L.; Song, X.; Abulikemu, M.; Basaheeh, A.; Jamal, A.; Gereige, I.; Freitag, M.; Mohammed, O. F.; Zhu, K.; Bakr, O. M., In situ energetics modulation enables high-efficiency and stable inverted perovskite solar cells. *Nat. Photonics* **2025,** *19* (1), 28-35.
6. Azmi, R.; Utomo, D. S.; Vishal, B.; Zhumagali, S.; Dally, P.; Risqi, A. M.; Prasetio, A.; Ugur, E.; Cao, F.; Imran, I. F.; Said, A. A.; Pininti, A. R.; Subbiah, A. S.; Aydin, E.; Xiao, C.; Seok, S. I.; De Wolf, S., Double-side 2D/3D heterojunctions for inverted perovskite solar cells. *Nature* **2024,** *628* (8006), 93-98.
7. Cheng, W.; Wu, S.; Lu, J.; Li, G.; Li, S.; Tian, W.; Li, L., Self-Powered Wide-Narrow Bandgap-Laminated Perovskite Photodetector with Bipolar Photoresponse for Secure Optical Communication. *Adv. Mater.* **2024,** *36* (5), 2307534.
8. Min, L.; Sun, H.; Guo, L.; Zhou, Y.; Wang, M.; Cao, F.; Li, L., Pyroelectric-Accelerated Perovskite Photodetector for Picosecond Light Detection and Ranging. *Adv. Mater.* **2024,** *36* (26), 2400279.
9. Kim, S. J.; Nam, G. B.; Kim, Y. J.; Eom, T. H.; Ryu, J.-E.; Kim, H. J.; Lee, H.-J.; Jang, H. W., Ambient Stable CsCu2I3 Flexible Gas Sensors for Reliable NO2 Detection at Room Temperature. *Nano Lett.* **2025**.
10. Pan, R.; Wang, K.; Li, Y.; Yu, H.; Li, J.; Xu, L., Spinterfaces Manipulate Large Magnetic Field Effects in 3D and Quasi-2D Organic–Inorganic Hybrid Perovskites. *Adv. Electron. Mater.* **2021,** *7* (5), 2100026.
11. Chen, A. X.; Beins, D. K. R.; Wang, Y.; Luo, H.-K.; Yang, Y. Y.; Li, N., Fast-Acting and Skin-Compatible Antimicrobial Coating on Cotton Fabrics via In Situ Self-Assembly of Phosphine-Coordinated

Copper Iodide Clusters. *ACS Appl. Eng. Mater.* **2024,** *2* (12), 2864-2874.
12. Rong, Y.; Hu, Y.; Mei, A.; Tan, H.; Saidaminov, M. I.; Seok, S. I.; McGehee, M. D.; Sargent, E. H.; Han, H., Challenges for commercializing perovskite solar cells. *Science* **2018,** *361* (6408), eaat8235.
13. Chen, C.; Zhang, L.; Ji, X.; Zhang, X.; Gong, Y.; Chen, R.; Mao, L., Guidelines for Designing Water-Stable Hybrid Lead Bromide Perovskites with Broad Emission. *Adv. Opt. Mater.* **2024,** *12* (7), 2301966.
14. Spanopoulos, I.; Hadar, I.; Ke, W.; Guo, P.; Sidhik, S.; Kepenekian, M.; Even, J.; Mohite, A. D.; Schaller, R. D.; Kanatzidis, M. G., Water-Stable 1D Hybrid Tin(II) Iodide Emits Broad Light with 36% Photoluminescence Quantum Efficiency. *J. Am. Chem. Soc.* **2020,** *142* (19), 9028-9038.
15. Azmy, A.; Li, S.; Angeli, G. K.; Welton, C.; Raval, P.; Li, M.; Zibouche, N.; Wojtas, L.; Reddy, G. N. M.; Guo, P.; Trikalitis, P. N.; Spanopoulos, I., Porous and Water Stable 2D Hybrid Metal Halide with Broad Light Emission and Selective H2O Vapor Sorption. *Angew. Chem. Int. Ed.* **2023,** *62* (12), e202218429.
16. Azmy, A.; Anderson, A. B.; Bagherifard, M.; Tariq, N.; Nassar, K. E. S.; Spanopoulos, I., When Pore Met Semi: Charting the Rise of Porous Metal Halide Semiconductors. *ACS Org. Inorg. Au* **2025,** *5* (2), 87-96.
17. Azmy, A.; Zhao, X.; Angeli, G. K.; Welton, C.; Raval, P.; Wojtas, L.; Zibouche, N.; Manjunatha Reddy, G. N.; Trikalitis, P. N.; Cai, J.; Spanopoulos, I., One-Year Water-Stable and Porous Bi(III) Halide Semiconductor with Broad-Spectrum Antibacterial Performance. *ACS Appl. Mater. Interfaces* **2023,** *15* (36), 42717-42729.
18. Hu, C.; Yao, Y.; Cannizzaro, J. P.; Garrett, M.; Harper, M.; Markley, L.; Villac, C.; Hubbard, K., Karenia brevis bloom patterns on the west Florida shelf between 2003 and 2019: Integration of field and satellite observations. *Harmful Algae* **2022,** *117*, 102289.
19. Chen, W.; Colon, R.; Louda, J. W.; del Rey, F. R.; Durham, M.; Rein, K. S., Brevetoxin (PbTx-2) influences the redox status and NPQ of Karenia brevis by way of thioredoxin reductase. *Harmful Algae* **2018,** *71*, 29-39.
20. Brown, A. R.; Lilley, M.; Shutler, J.; Lowe, C.; Artioli, Y.; Torres, R.; Berdalet, E.; Tyler, C. R., Assessing risks and mitigating impacts of harmful algal blooms on mariculture and marine fisheries. *Rev. Aquac.* **2020,** *12* (3), 1663-1688.
21. Colon, R.; Wheater, M.; Joyce, E. J.; Ste.Marie, E. J.; Hondal, R. J.; Rein, K. S., The Marine Neurotoxin Brevetoxin (PbTx-2) Inhibits Karenia brevis and Mammalian Thioredoxin Reductases by Targeting Different Residues. *J. Nat. Prod.* **2021,** *84* (11), 2961-2970.
22. Sellner, K. G.; Doucette, G. J.; Kirkpatrick, G. J., Harmful algal blooms: causes, impacts and detection. *J. Ind. Microbiol. Biotechnol.* **2003,** *30* (7), 383-406.
23. Roth, P. B.; Twiner, M. J.; Mikulski, C. M.; Barnhorst, A. B.; Doucette, G. J., Comparative analysis of two algicidal bacteria active against the red tide dinoflagellate Karenia brevis. *Harmful Algae* **2008,** *7* (5), 682-691.
24. Tang, Y. Z.; Kang, Y.; Berry, D.; Gobler, C. J., The ability of the red macroalga, Porphyra purpurea (Rhodophyceae) to inhibit the proliferation of seven common harmful microalgae. *J. Appl. Phycol.* **2015,** *27* (1), 531-544.
25. Song, X.; Zhang, Y.; Yu, Z., An eco-environmental assessment of harmful algal bloom mitigation using modified clay. *Harmful Algae* **2021,** *107*, 102067.
26. Park, J.; Son, Y.; Lee, W. H., Variation of efficiencies and limits of ultrasonication for practical algal bloom control in fields. *Ultrason. Sonochem.* **2019,** *55*, 8-17.
27. Hossain, I.; Mays, B.; Hanhart, S. L.; Hubble, J.; Azizihariri, P.; McLean, T. I.; Pierce, R.; Lovko, V.; John, V. T., An effective algaecide for the targeted destruction of Karenia brevis. *Harmful Algae* **2024,** *138*, 102707.
28. Moreno-Andrés, J.; Romero-Martínez, L.; Seoane, S.; Acevedo-Merino, A.; Moreno-Garrido, I.; Nebot, E., Evaluation of algaecide effectiveness of five different oxidants applied on harmful phytoplankton. *J. Hazard. Mater.* **2023,** *452*, 131279.
29. Khan, N.; Bhowmik, P. P.; Sarker, M. S.; Yang, H.; Li, R.; Liu, J., Impact of water quality parameters on harmful algal bloom mitigation and phosphorus removal by lab-synthesized γFe2O3/TiO2 magnetic photocatalysts. *Algal Res.* **2025,** *86*, 103932.
30. Hu, J.; Berthold, D. E.; Wang, Y.; Xiao, X.; Laughinghouse, H. D., Treatment of the red tide dinoflagellate Karenia brevis and brevetoxins using USEPA-registered algaecides. *Harmful Algae* **2022,** *120*, 102347.
31. Liu, N.; Wen, F.; Li, F.; Zheng, X.; Liang, Z.; Zheng, H., Inhibitory mechanism of phthalate esters on Karenia brevis. *Chemosphere* **2016,** *155*, 498-508.
32. Bruker, APEX4. Bruker AXS LLC, Madison, Wisconsin, USA. **2022**.

33. Bruker, SAINT. Bruker AXS LLC, Madison, Wisconsin, USA. **2022**.
34. Krause, L.; Herbst-Irmer, R.; Sheldrick, G. M.; Stalke, D., Comparison of Silver and Molybdenum Microfocus X-ray Sources for Single-crystal Structure Determination. *J Appl Crystallogr* **2015,** *48* (Pt 1), 3-10.
35. Sheldrick, G., SHELXT - Integrated Space-group and Crystal-structure Determination. *Acta Crystallogr. Sect. A* **2015,** *71* (1), 3-8.
36. Sheldrick, G., Crystal Structure Refinement with SHELXL. *Acta Crystallogr. Sect. C* **2015,** *71* (1), 3-8.
37. Dolomanov, O. V.; Bourhis, L. J.; Gildea, R. J.; Howard, J. A. K.; Puschmann, H., OLEX2: a Complete Structure Solution, Refinement and Analysis Program. *J. Appl. Crystallogr.* **2009,** *42* (2), 339-341.
38. Spek, A., Single-crystal Structure Validation with the Program PLATON. *J. Appl. Crystallogr.* **2003,** *36* (1), 7-13.
39. Thomas, N., Crystal structure-physical property relationships in perovskites. *Acta Crystallogr. Sect. B* **1989,** *45* (4), 337-344.
40. Gate, L. F., Comparison of the Photon Diffusion Model and Kubelka-Munk Equation with the Exact Solution of the Radiative Transport Equation. *Appl. Opt.* **1974,** *13* (2), 236-238.
41. Giannozzi, P.; Andreussi, O.; Brumme, T.; Bunau, O.; Buongiorno Nardelli, M.; Calandra, M.; Car, R.; Cavazzoni, C.; Ceresoli, D.; Cococcioni, M.; Colonna, N.; Carnimeo, I.; Dal Corso, A.; de Gironcoli, S.; Delugas, P.; DiStasio, R. A.; Ferretti, A.; Floris, A.; Fratesi, G.; Fugallo, G.; Gebauer, R.; Gerstmann, U.; Giustino, F.; Gorni, T.; Jia, J.; Kawamura, M.; Ko, H. Y.; Kokalj, A.; Küçükbenli, E.; Lazzeri, M.; Marsili, M.; Marzari, N.; Mauri, F.; Nguyen, N. L.; Nguyen, H. V.; Otero-de-la-Roza, A.; Paulatto, L.; Poncé, S.; Rocca, D.; Sabatini, R.; Santra, B.; Schlipf, M.; Seitsonen, A. P.; Smogunov, A.; Timrov, I.; Thonhauser, T.; Umari, P.; Vast, N.; Wu, X.; Baroni, S., Advanced Capabilities for Materials Modelling with Quantum ESPRESSO. *Phys.: Condens. Matter* **2017,** *29* (46), 465901.
42. Giannozzi, P.; Baroni, S.; Bonini, N.; Calandra, M.; Car, R.; Cavazzoni, C.; Ceresoli, D.; Chiarotti, G. L.; Cococcioni, M.; Dabo, I.; Dal Corso, A.; de Gironcoli, S.; Fabris, S.; Fratesi, G.; Gebauer, R.; Gerstmann, U.; Gougoussis, C.; Kokalj, A.; Lazzeri, M.; Martin-Samos, L.; Marzari, N.; Mauri, F.; Mazzarello, R.; Paolini, S.; Pasquarello, A.; Paulatto, L.; Sbraccia, C.; Scandolo, S.; Sclauzero, G.; Seitsonen, A. P.; Smogunov, A.; Umari, P.; Wentzcovitch, R. M., QUANTUM ESPRESSO: a Modular and Open-source Software Project for Quantum Simulations of Materials. *J. Phys.: Condens. Matter* **2009,** *21* (39), 395502.
43. Perdew, J. P.; Burke, K.; Ernzerhof, M., Generalized Gradient Approximation Made Simple. *Phys. Rev. Lett.* **1996,** *77* (18), 3865-3868.
44. Perdew, J. P.; Ruzsinszky, A.; Csonka, G. I.; Vydrov, O. A.; Scuseria, G. E.; Constantin, L. A.; Zhou, X.; Burke, K., Restoring the Density-Gradient Expansion for Exchange in Solids and Surfaces. *Phys. Rev. Lett.* **2008,** *100* (13), 136406.
45. Grimme, S.; Antony, J.; Ehrlich, S.; Krieg, H., A Consistent and Accurate ab initio Parametrization of Density Functional Dispersion Correction (DFT-D) for the 94 elements H-Pu. *J. Chem. Phys.* **2010,** *132* (15), 154104.
46. Grimme, S.; Ehrlich, S.; Goerigk, L., Effect of the Damping Function in Dispersion Corrected Density Functional Theory. *J. Comput. Chem.* **2011,** *32* (7), 1456-1465.
47. Vanderbilt, D., Soft Self-consistent Pseudopotentials in a Generalized eigenvalue Formalism. *Phys. Rev. B* **1990,** *41* (11), 7892-7895.
48. Monkhorst, H. J.; Pack, J. D., Special Points for Brillouin-zone Integrations. *Phys. Rev. B* **1976,** *13* (12), 5188-5192.
49. Dalley, N. K.; Krakowiak, K. E.; Bradshaw, J. S.; England, M. M.; Kou, X.; M. Izati, R., Crystal structure of the cryptand [3.33] - potassium iodide complex: A large coordination number for potassium ion. *Tetrahedron* **1994,** *50* (9), 2721-2728.
50. Li, X.; Traoré, B.; Kepenekian, M.; Li, L.; Stoumpos, C. C.; Guo, P.; Even, J.; Katan, C.; Kanatzidis, M. G., Bismuth/Silver-Based Two-Dimensional Iodide Double and One-Dimensional Bi Perovskites: Interplay between Structural and Electronic Dimensions. *Chem. Mater.* **2021,** *33* (15), 6206-6216.
51. Lehner, A. J.; Fabini, D. H.; Evans, H. A.; Hébert, C.-A.; Smock, S. R.; Hu, J.; Wang, H.; Zwanziger, J. W.; Chabinyc, M. L.; Seshadri, R., Crystal and Electronic Structures of Complex Bismuth Iodides $A_3Bi_2I_9$ (A = K, Rb, Cs) Related to Perovskite: Aiding the Rational Design of Photovoltaics. *Chem. Mater.* **2015,** *27* (20), 7137-7148.
52. Crace, E. J.; Singh, A.; Haley, S.; Claes, B.; Mitzi, D. B., Meltable Hybrid Antimony and Bismuth Iodide One-Dimensional Perovskites. *Inorg. Chem.* **2023,** *62* (39), 16161-16169.

53. Skorokhod, A.; Mercier, N.; Allain, M.; Manceau, M.; Katan, C.; Kepenekian, M., From Zero- to One-Dimensional, Opportunities and Caveats of Hybrid Iodobismuthates for Optoelectronic Applications. *Inorg. Chem.* **2021,** *60* (22), 17123-17131.
54. Spanopoulos, I.; Ke, W.; Stoumpos, C. C.; Schueller, E. C.; Kontsevoi, O. Y.; Seshadri, R.; Kanatzidis, M. G., Unraveling the Chemical Nature of the 3D "Hollow" Hybrid Halide Perovskites. *J. Am. Chem. Soc.* **2018,** *140* (17), 5728-5742.
55. Kong, M.; Hu, H.; Wan, L.; Chen, M.; Gan, Y.; Wang, J.; Chen, F.; Dong, B.; Eder, D.; Wang, S., Nontoxic $(CH_3NH_3)_3Bi_2I_9$ Perovskite Solar Cells free of Hole Conductors with an Alternative Architectural Design and a Solution-processable Approach. *RSC Advances* **2017,** *7* (56), 35549-35557.
56. Peng, Y.-C.; Jin, J.-C.; Zhou, S.-H.; Lin, H.-W.; Huang, D.-D.; Deng, Z.-H.; Dong, Y.; Xu, H.-J.; Du, K.-Z.; Wang, Z.-P.; Huang, X.-Y., Regulating photoluminescence through single-crystal-to-single-crystal transformation of solvent-containing zero-dimensional hybrid metal halide isomers. *Chem. Eng. J.* **2024,** *488*, 151026.
57. Li, D.-Y.; Wu, J.-H.; Wang, X.-Y.; Zhang, X.-Y.; Yue, C.-Y.; Lei, X.-W., Reversible Triple-Mode Photo- and Radioluminescence and Nonlinear Optical Switching in Highly Efficient 0D Hybrid Cuprous Halides. *Chem. Mater.* **2023,** *35* (17), 6598-6611.
58. Yuan, J.; Zhang, N.; Zhang, J.; Zhang, X.-M., Rearrangement of Sb···Br Secondary Bonds Resulting in Reversible Transformation between Dimeric and Chain-Like Antimony Bromide Hybrid Materials: Tunability of Electron Self-Trapped Luminescence and Proton Conductivity. *Inorg. Chem.* **2025,** *64* (23), 11767-11777.
59. Zhang, Y.; Ghasemi, M.; Wen, X.; Lee, M.; Liu, X.; Jiao, Y.; Bernhardt, P. V.; Han, E. Q.; Lin, T.; Zhang, B. W.; Xu, K.; Lee, S.-M.; Yun, J. S.; Yun, J.-H.; Wang, L., Reversible structural transformation of metastable lead-free organic–inorganic hybrid bismuth halide single crystals. *J. Mater. Chem. A* **2024,** *12* (42), 29152-29164.
60. Kandel, R.; Schatte, G.; Cheng, G.; Palmer, C.; Beauchemin, D.; Wang, P. L., Stabilization and Solvent Driven Crystal-to-Crystal Transition between New Bismuth Halides. *Inorg. Chem.* **2020,** *59* (10), 7049-7055.
61. Bon, V.; Senkovska, I.; Baburin, I. A.; Kaskel, S., Zr- and Hf-Based Metal–Organic Frameworks: Tracking Down the Polymorphism. *Cryst. Growth Des.* **2013,** *13* (3), 1231-1237.
62. Stoumpos, C. C.; Kanatzidis, M. G., The Renaissance of Halide Perovskites and Their Evolution as Emerging Semiconductors. *Acc. Chem. Res.* **2015,** *48* (10), 2791-2802.
63. Rowinska, M. N.; Korolevych, O.; Kabański, A.; Stefanska, D.; Bednarchuk, T.; Piecha-Bisiorek, A.; Gagor, A., Hybrid Bismuth(III)-Halide Double Perovskite-Derived Ferroelastic (Pip)2[KBiBr6] with Excitonic and Bi(III) Luminescence due to Electronic Confinement along Inorganic Pillars. *Chem. Mater.* **2025,** *37* (18), 7125-7135.
64. Zhang, L.; Liu, C.; Lin, Y.; Wang, K.; Ke, F.; Liu, C.; Mao, W. L.; Zou, B., Tuning Optical and Electronic Properties in Low-Toxicity Organic–Inorganic Hybrid $(CH_3NH_3)3Bi_2I_9$ under High Pressure. *J. Phys. Chem. Lett.* **2019,** *10* (8), 1676-1683.
65. Zeng, J.; Li, Z.; Jiang, H.; Wang, X., Progress on photocatalytic semiconductor hybrids for bacterial inactivation. *Mater. Horiz.* **2021,** *8* (11), 2964-3008.
66. Li, F.; Liang, Z.; Zheng, X.; Zhao, W.; Wu, M.; Wang, Z., Toxicity of nano-TiO2 on algae and the site of reactive oxygen species production. *Aquat. Toxicol.* **2015,** *158*, 1-13.
67. Lauritano, C.; De Luca, D.; Amoroso, M.; Benfatto, S.; Maestri, S.; Racioppi, C.; Esposito, F.; Ianora, A., New molecular insights on the response of the green alga Tetraselmis suecica to nitrogen starvation. *Sci. Rep.* **2019,** *9* (1), 3336.
68. Sukarni; Sudjito; Hamidi, N.; Yanuhar, U.; Wardana, I. N. G., Potential and properties of marine microalgae Nannochloropsis oculata as biomass fuel feedstock. *Int. J. Energy Environ. Eng.* **2014,** *5* (4), 279-290.
69. Norris, R. E.; Hori, T.; Chihara, M., Revision of the genusTetraselmis (Class Prasinophyceae). *The botanical magazine = Shokubutsu-gaku-zasshi* **1980,** *93* (4), 317-339.
70. Delran, P.; Frances, C.; Peydecastaing, J.; Pontalier, P.-Y.; Guihéneuf, F.; Barthe, L., Cell destruction level and metabolites green-extraction of Tetraselmis suecica by low and intermediate frequency ultrasound. *Ultrason. Sonochem.* **2023,** *98*, 106492.
71. Emam, K. R. S.; Ali, S. A. M.; Morsy, A. S.; Fouda, W. A.; Elbaz, A. M., Role of Nannochloropsis Oculata supplement in improving performance, antioxidant status, blood metabolites, and egg quality of laying hens under hot environmental conditions. *Sci. Rep.* **2024,** *14* (1), 16884.
72. Pérez-López, P.; González-García, S.; Ulloa, R. G.; Sineiro, J.; Feijoo, G.; Moreira, M. T., Life cycle

assessment of the production of bioactive compounds from Tetraselmis suecica at pilot scale. *J. Clean. Prod.* **2014,** *64*, 323-331.
73. Sansone, C.; Galasso, C.; Orefice, I.; Nuzzo, G.; Luongo, E.; Cutignano, A.; Romano, G.; Brunet, C.; Fontana, A.; Esposito, F.; Ianora, A., The green microalga Tetraselmis suecica reduces oxidative stress and induces repairing mechanisms in human cells. *Sci. Rep.* **2017,** *7* (1), 41215.
74. Gkioni, M. D.; Andriopoulos, V.; Koutra, E.; Hatziantoniou, S.; Kornaros, M.; Lamari, F. N., Ultrasound-Assisted Extraction of Nannochloropsis oculata with Ethanol and Betaine: 1,2-Propanediol Eutectic Solvent for Antioxidant Pigment-Rich Extracts Retaining Nutritious the Residual Biomass. *Antioxidants* **2022,** *11* (6), 1103.
75. Miller-Morey, J. S.; Van Dolah, F. M., Differential responses of stress proteins, antioxidant enzymes, and photosynthetic efficiency to physiological stresses in the Florida red tide dinoflagellate, Karenia brevis. *Comparative Biochemistry and Physiology Part C: Toxicology & Pharmacology* **2004,** *138* (4), 493-505.
76. Li, F.-m.; Wu, M.; Yao, Y.; Zheng, X.; Zhao, J.; Wang, Z.-y.; Xing, B.-s., Inhibitory effects and oxidative target site of dibutyl phthalate on Karenia brevis. *Chemosphere* **2015,** *132*, 32-39.

TOC Graphic

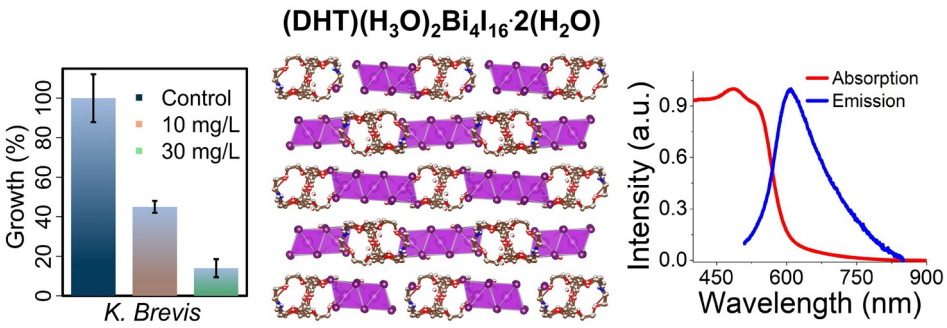
(DHT)(H3O)2Bi4I16·2(H2O)
Growth (%)
0
20
40
60
80
100
Control
10 mg/L
30 mg/L
K. Brevis
Absorption
Emission
Intensity (a.u.)
0.0
0.3
0.6
0.9
450
600
750
900
Wavelength (nm)

Supporting information

Unravelling the Impact of Porosity on Water Stability of Porous Bi(III) Halide Semiconductors and Their Potential for Red Tide Mitigation

Ali Azmy,[1,#] Alissa Brooke Anderson,[1,#] Anamika Mishra,[1] Enlin Lo,[2] Neelam Tariq,[1] Ioannis N. Gkikas,[1] Brandon Sauval,[1] Nicholas Giunto,[1] Amrit Kaur,[1] Stephanie Krzypkowski,[1] Nourdine Zibouche,[3] George P. Philippidis[4] and Ioannis Spanopoulos*,[1]

[1]*Department of Chemistry, University of South Florida, Tampa, Florida 33620, USA*
[2]*Department of Molecular Biosciences, University of South Florida, Tampa, Florida 33620, USA*
[3]*Department of Chemistry, University of Lancaster, Lancaster, LA1 4YW, UK*
[4]*Department of Integrative Biology and Patel College of Global Sustainability, University of South Florida, Tampa, Florida 33620, USA*

Corresponding author: spanopoulos@usf.edu

Table of contents

Section S1. Organic Synthesis
- NMR measurements
- LC-MS measurements

Section S2. Material Synthesis
Section S3. Characterization
a. X-ray diffraction measurements
b. SEM/EDS studies
c. Thermogravimetric analysis
d. PXRD studies
e. DFT studies
f. TRPL measurements
g. ROS studies

Section S4. References

S1. Organic synthesis

Synthesis of 1-iodo-2-(2-(2-(2-iodoethoxy) ethoxy)ethoxy)ethane

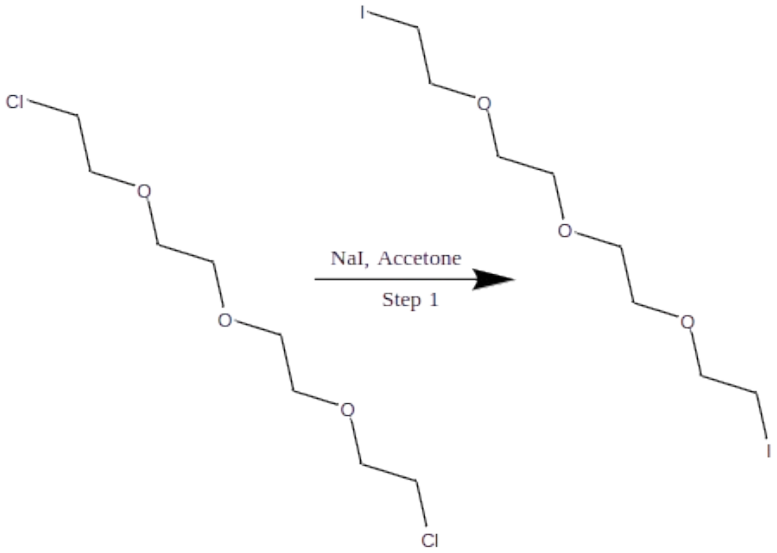

Reaction Scheme 1. Synthesis of the diiodo precursor from the dichloro precursor.

Synthesis of 1-iodo-2-(2-(2-(2-iodoethoxy) ethoxy)ethoxy)ethane:
1-chloro-2-(2-(2-(2-chloroethoxy)ethoxy)ethoxy)ethane (5.0 g, 21.6 mmol) was dissolved in acetone (250 mL). Sodium iodide NaI (8.0 g) was added, and the mixture was heated under reflux for 72 hours. After cooling to room temperature, the excess NaI was filtered out and the solvent was recovered through rotary evaporation. The recovered solvent was washed with brine, sodium thiosulphate solution and ethyl acetate. The ethyl acetate layer was collected and evaporated to obtain a pale yellow liquid as 1-iodo-2-(2-(2-(2-iodoethoxy)ethoxy)ethoxy)ethane (8.96g, 98% yield). The transformation of the dichloro compound into its diiodo precursor was confirmed using HNMR. ^{1}H-NMR of dichloro precursor ($CDCl_3$, 600 MHz, RT): δ = 3.54, 3.57, 3.66 (16H) ppm (Figure S1), ^{1}H-NMR of diiodo precursor ($CDCl_3$, 600 MHz, RT): δ = 3.18, 3.58, 3.67 (16H) ppm (Figure S2).

Synthesis of [3.3.3] Cryptand (DHT)

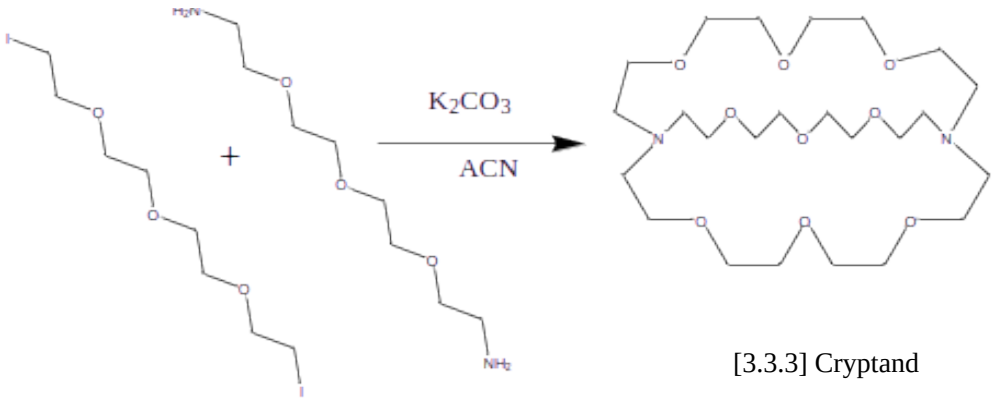

[3.3.3] Cryptand

Reaction Scheme 2. Synthesis of [3.3.3] Cryptand (DHT).

Synthesis of [3.3.3] Cryptand (DHT): In a dry round bottom flask 2,2'-(oxybis(2,1-ethanediyloxy)) bis[bisethanamine] (1.00 g, 5.20 mmol) dissolved in dry acetonitrile (150 mL) at room temperature. The as-synthesized 1-iodo-2-(2-(2-(2-iodoethoxy) ethoxy) ethoxy) ethane (4.36 g, 10.5 mmol) was added to this solution, followed by the addition of K_2CO_3 (15 g). The reaction mixture was heated under reflux for 72 hours. After cooling to room temperature, excess K_2CO_3 was filtered out, and the solvent was recovered under reduced pressure using rotary evaporation. The semi-solid crude material was recrystallized from Ethanol/THF (2:50) to obtain pure white powder (1.08 g, 58 %). ^{1}H-NMR ($CDCl_3$, 600 MHz, RT): δ = 2.57 (m, 12H), 3.54 (t, 12H), 3.60 (m, 24H) ppm (Figure S3). ^{13}C-NMR ($CDCl_3$, 600, MHz, RT): δ = 69.44, 69.31, 67.11, 54.13 ppm (Figure S4).

1. **NMR Measurements**

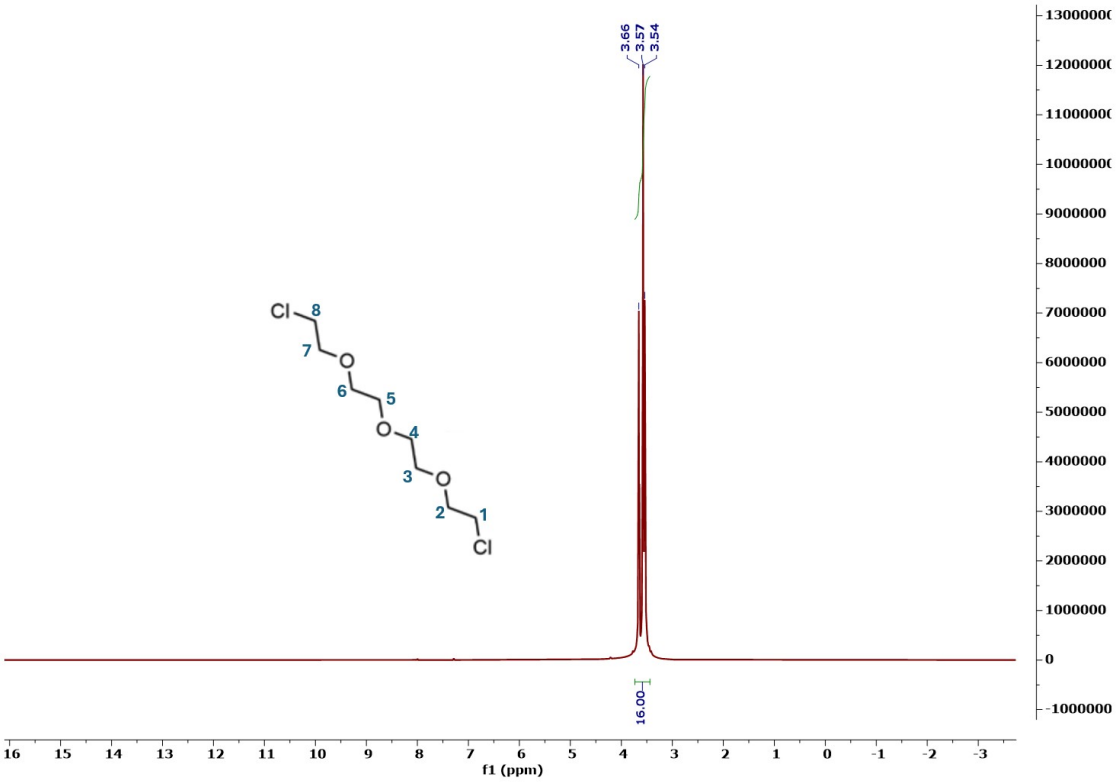

Figure S1. ^{1}H-NMR of dichloro precursor in $CDCl_3$.

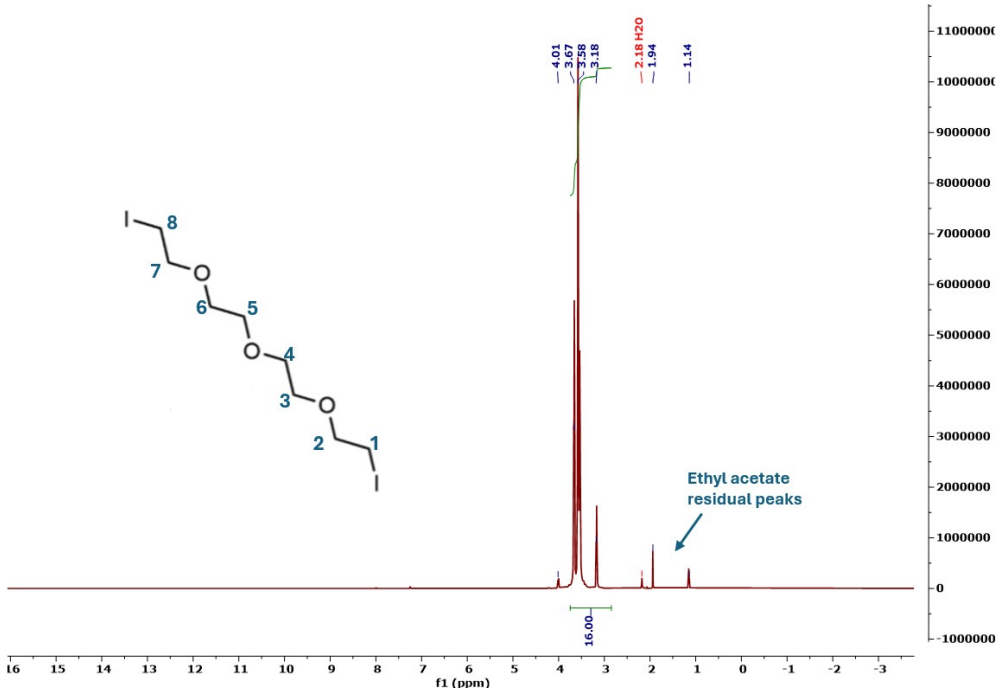

Figure S2. ^{1}H-NMR of diiodo precursor in $CDCl_3$.

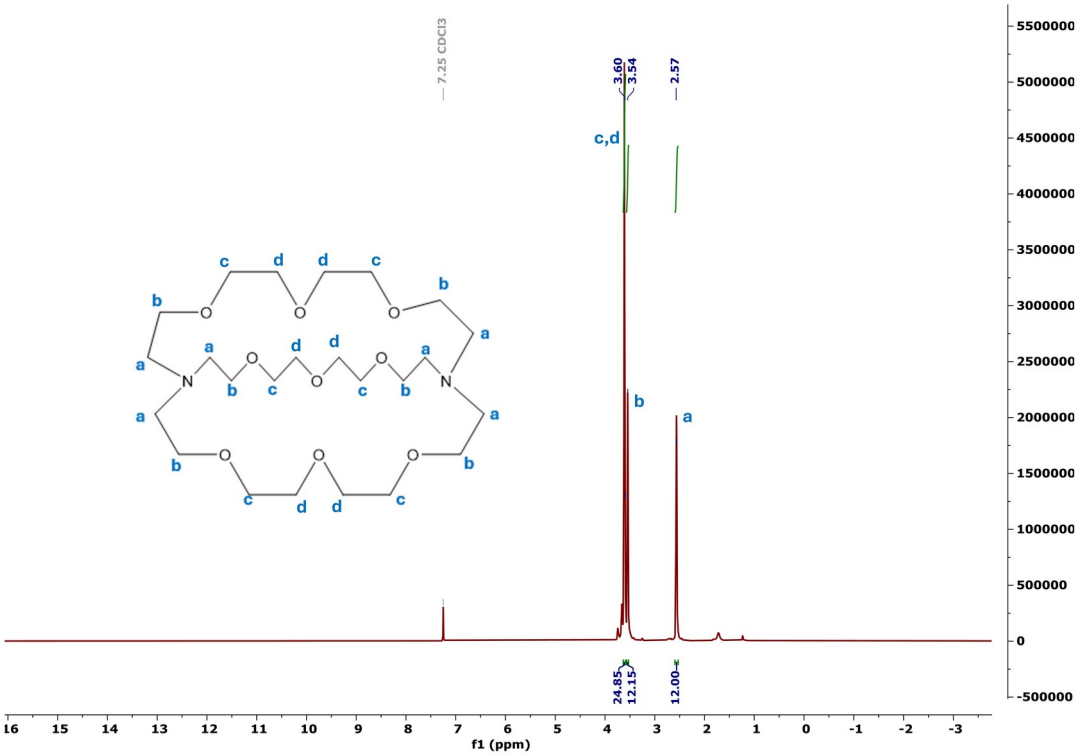

Figure S3. ^{1}H-NMR of DHT in $CDCl_3$.

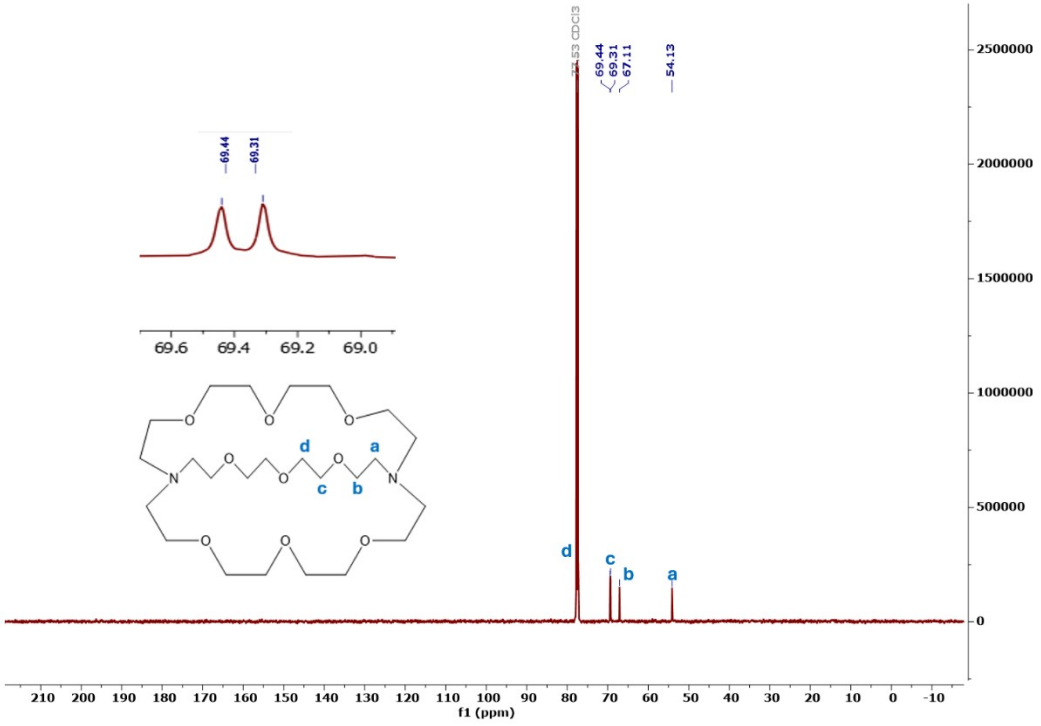

Figure S4. ^{13}C-NMR of DHT in $CDCl_3$.

2. LC-MS Measurements

1 mg of the compound was dissolved in 1 ml of methanol to find a clear solution. It was

filtered, and an LC-MS experiment was performed. Observed MS (LC-MS) m/z = 509.4 (64%), [M+H] = 255.3 (100%) Base peak (Figure S5).

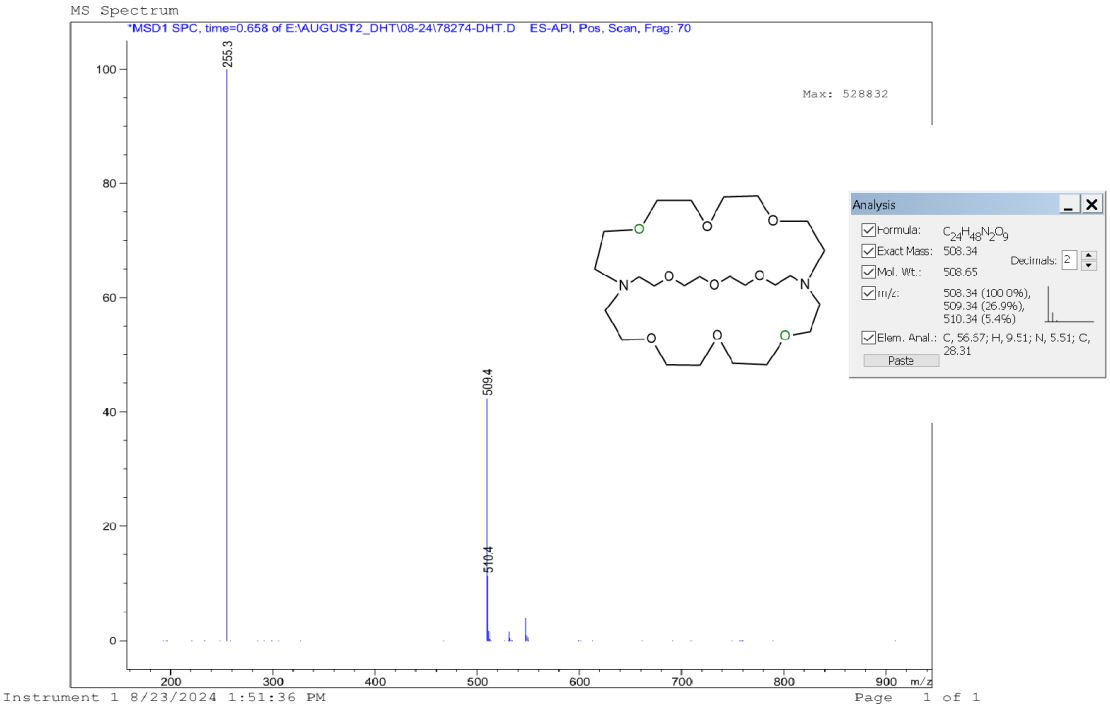

Figure S5. LC-MS spectrum of DHT in methanol.

S2. Material synthesis

(DHS)Bi_2I_8: 377 mg (1 mmol) of DHS linker were dissolved in a solution consisting of 8 mL of 57 wt. % HI and 2 mL of 50 wt % H_3PO_2, by heating under constant magnetic stirring. Then 932 mg (2 mmol) of Bi_2O_3 were added to the hot colorless solution. Heating was discontinued and the sample was left to cool to RT directly. Dark orange crystals deposited after 10 min. They were collected by suction filtration and dried under vacuum overnight.

(DHT)$(H_3O)_2Bi_4I_{16}$·2(H_2O): 127 mg (0.25 mmol) of DHT linker were dissolved in a solution consisting of 2 mL of 57 wt. % HI, by heating under constant magnetic stirring. Then 233 mg (0.5 mmol) of Bi_2O_3 were added to the hot colorless solution. Heating was discontinued and the sample was left to cool to RT directly. Dark orange crystals deposited after 10 min. They were collected by suction filtration and dried under vacuum overnight.

S3. Characterization

X-ray diffraction measurements

Crystallographic tables

Table S1. Atomic coordinates ($x10^4$) and equivalent isotropic displacement parameters ($Å^2x10^3$) for $(DHT)(H_3O)_2Bi_4I_{16}·2(H_2O)$ at 298.00 K with estimated standard deviations in parentheses.

Label	x	y	z	Occu-pancy	U_{eq}*
Bi(1)	0	5000	10404(1)	1	48(1)
Bi(2)	-101(1)	2801(1)	8458(1)	1	49(1)
Bi(3)	0	5000	6558(1)	1	46(1)
I(1)	-1289(2)	3706(1)	6713(2)	1	61(1)
I(2)	-1086(2)	5752(2)	5068(2)	1	81(1)
I(3)	1136(1)	4243(1)	8463(2)	1	46(1)
I(4)	1157(2)	4320(2)	11882(2)	1	88(1)
I(5)	-1142(2)	3621(1)	10351(2)	1	60(1)
I(6)	-1534(1)	1715(1)	8442(2)	1	76(1)
I(7)	918(2)	2140(2)	6796(2)	1	76(1)
I(8)	1005(2)	2119(2)	10014(2)	1	79(1)
N(1)	4060(20)	2830(20)	8340(30)	0.5	68(9)
H(1)	4184.21	3347.13	8407.9	0.5	82
N(2)	5825(17)	6999(18)	8380(20)	0.5	46(7)
H(2)	5570.46	6510.94	8349.82	0.5	56
C(3)	4890(20)	2590(30)	7880(40)	0.5	76(11)
H(3A)	4966.24	2859.08	7249.21	0.5	91
H(3B)	4820.03	2083.98	7697.09	0.5	91
C(4)	5710(20)	2660(20)	8490(60)	0.5	70(11)
H(4A)	5593.88	2549.84	9197.96	0.5	84
H(4B)	6153.56	2331.92	8230.26	0.5	84
O(5)	5990(20)	3380(20)	8380(40)	0.5	62(10)
C(6)	6780(20)	3523(19)	8860(30)	0.5	46(7)
H(6A)	7239.75	3233.95	8555.48	0.5	55
H(6B)	6731.59	3386.35	9579.19	0.5	55
C(7)	7000(30)	4280(20)	8790(40)	0.5	68(10)
H(7A)	7127.42	4393.49	8082.85	0.5	81
H(7B)	7538.46	4363.28	9180.87	0.5	81

O(8)	6320(30)	4767(19)	9160(30)	0.5	68(9)
C(9)	6410(30)	4838(16)	10240(30)	0.5	73(10)
H(9A)	6794.64	4460.88	10495.97	0.5	87
H(9B)	5836.59	4786.37	10562.76	0.5	87
C(10)	6800(30)	5585(15)	10480(40)	0.5	75(11)
H(10A)	6795.73	5673.09	11206.9	0.5	91
H(10B)	7399.41	5618.99	10227.76	0.5	91
O(11)	6250(40)	6098(15)	9960(50)	0.5	86(17)
C(12)	6520(40)	6808(16)	10110(40)	0.5	59(11)
H(12A)	7118.86	6874.25	9874.07	0.5	70
H(12B)	6489.17	6936.11	10830.6	0.5	70
C(13)	5900(30)	7261(18)	9500(20)	0.5	59(8)
H(13A)	6095.98	7760.41	9513.08	0.5	71
H(13B)	5316.22	7244.45	9819.23	0.5	71
C(23)	3280(30)	2850(30)	7620(30)	0.5	82(12)
H(23A)	3162.62	2368.16	7364.78	0.5	99
H(23B)	2763.77	3012.75	7997.75	0.5	99
C(24)	3440(50)	3340(20)	6770(40)	0.5	92(15)
H(24A)	3922.69	3155.98	6357.91	0.5	110
H(24B)	2915.69	3354.66	6335.82	0.5	110
O(25)	3640(50)	4050(20)	7100(30)	0.5	85(12)
C(26)	3580(30)	4550(20)	6290(30)	0.5	92(11)
H(26A)	3350.93	5007.51	6540.7	0.5	110
H(26B)	3168.51	4367.57	5777.88	0.5	110
C(27)	4450(20)	4670(30)	5810(30)	0.5	83(10)
H(27A)	4613.84	4232.83	5443.88	0.5	100
H(27B)	4388.6	5055.02	5306.17	0.5	100
O(28)	5140(20)	4860(20)	6500(20)	0.5	86(11)
C(29)	6000(30)	4940(20)	5980(30)	0.5	88(11)
H(29A)	5965.41	4739.67	5296.79	0.5	106
H(29B)	6452.55	4681.82	6358	0.5	106
C(30)	6190(40)	5720(20)	5950(30)	0.5	98(15)
H(30A)	6733.58	5786.1	5565.69	0.5	117
H(30B)	5723.01	5956.38	5567.06	0.5	117
O(31)	6280(50)	6070(30)	6870(30)	0.5	110(20)
C(32)	6770(40)	6710(30)	6900(30)	0.5	81(16)
H(32A)	6541.55	7056.72	6405.65	0.5	97
H(32B)	7384.86	6611.73	6721.15	0.5	97

C(33)	6720(20)	7010(20)	7930(20)	0.5	57(8)
H(33A)	6927.99	7511.31	7907.99	0.5	68
H(33B)	7119.99	6743.39	8367.31	0.5	68
C(43)	3790(30)	2650(20)	9380(30)	0.5	82(11)
H(43A)	4288.06	2449.54	9752.1	0.5	99
H(43B)	3329.32	2287.39	9361.56	0.5	99
C(44)	3450(40)	3320(30)	9960(50)	0.5	87(17)
H(44A)	2898.33	3471.92	9652.44	0.5	104
H(44B)	3326.81	3179.31	10662.39	0.5	104
O(45)	4030(30)	3880(20)	9950(50)	0.5	84(12)
C(46)	3810(40)	4440(20)	10600(30)	0.5	90(11)
H(46A)	4342.11	4658.82	10861.75	0.5	108
H(46B)	3478.28	4246.95	11172.95	0.5	108
C(47)	3260(30)	5010(20)	10090(40)	0.5	94(14)
H(47A)	2759.85	4790.18	9764.88	0.5	113
H(47B)	3044.52	5344.88	10611.16	0.5	113
O(48)	3750(30)	5416(19)	9350(30)	0.5	80(12)
C(49)	3150(30)	5790(20)	8680(40)	0.5	97(16)
H(49A)	2549.89	5709	8892.67	0.5	117
H(49B)	3221.47	5604.36	7988.58	0.5	117
C(50)	3350(30)	6570(20)	8690(60)	0.5	94(19)
H(50A)	2910.41	6827.9	8292.53	0.5	113
H(50B)	3316.26	6748.92	9390.81	0.5	113
O(51)	4200(30)	6720(20)	8290(50)	0.5	78(15)
C(52)	4310(20)	7483(19)	8230(40)	0.5	66(14)
H(52A)	4245.1	7709.08	8896.55	0.5	80
H(52B)	3893.84	7697.32	7757.87	0.5	80
C(53)	5220(20)	7550(30)	7850(40)	0.5	71(10)
H(53A)	5440.07	8037.96	7983.09	0.5	86
H(53B)	5235.67	7470.14	7119.56	0.5	86
O(1S)	4850(20)	4704(16)	8450(30)	0.5	82(8)
O(2S)	3570(20)	931(18)	8490(40)	0.5	98(9)
O(3S)	1960(50)	350(40)	8400(90)	0.25	102(19)
O(4S)	610(50)	440(40)	8090(50)	0.25	100(20)

*U_{eq} is defined as one third of the trace of the orthogonalized U_{ij} tensor.

Table S2. Anisotropic displacement parameters ($Å^2x10^3$) for $(DHT)(H_3O)_2Bi_4I_{16}·2(H_2O)$ at 298.00 K with estimated standard deviations in parentheses.

Label	U_{11}	U_{22}	U_{33}	U_{12}	U_{13}	U_{23}
Bi(1)	68(1)	37(1)	39(1)	-3(1)	0	0
Bi(2)	62(1)	32(1)	53(1)	-3(1)	0(1)	-2(1)
Bi(3)	65(1)	38(1)	36(1)	0(1)	0	0
I(1)	72(1)	45(1)	67(1)	-13(1)	-9(1)	4(1)
I(2)	108(2)	71(1)	65(1)	2(1)	-26(2)	17(1)
I(3)	53(1)	38(1)	47(1)	-3(1)	-2(1)	0(1)
I(4)	114(2)	79(2)	70(2)	-12(1)	-36(2)	26(1)
I(5)	66(1)	44(1)	69(1)	-9(1)	7(1)	-5(1)
I(6)	89(1)	50(1)	87(1)	-26(1)	-6(2)	1(1)
I(7)	93(2)	68(1)	67(1)	11(1)	10(1)	-13(1)
I(8)	92(2)	68(1)	78(2)	10(1)	-17(1)	14(1)
N(1)	68(14)	45(18)	91(17)	4(11)	-8(12)	-16(12)
N(2)	54(12)	43(14)	42(11)	-10(8)	13(9)	3(9)
C(3)	65(13)	70(20)	100(20)	2(11)	-13(12)	-21(16)
C(4)	63(14)	57(18)	90(30)	6(10)	-10(16)	-12(15)
O(5)	53(13)	49(15)	80(20)	9(10)	-25(16)	-8(14)
C(6)	45(13)	57(15)	35(13)	6(10)	-2(11)	-4(11)
C(7)	53(15)	56(15)	90(20)	3(11)	-3(13)	-6(12)
O(8)	57(16)	53(16)	94(17)	7(12)	1(12)	-8(11)
C(9)	90(20)	35(12)	96(17)	4(12)	0(13)	1(10)
C(10)	110(20)	39(11)	80(20)	-2(12)	-13(19)	6(10)
O(11)	130(30)	30(11)	100(30)	-7(11)	-50(30)	-7(10)
C(12)	90(20)	31(11)	52(16)	-4(11)	-13(16)	-14(9)
C(13)	79(19)	44(13)	53(12)	1(12)	12(10)	2(9)
C(23)	69(16)	80(20)	90(20)	4(13)	-8(14)	-11(15)
C(24)	100(40)	87(18)	90(20)	-5(16)	-17(18)	-12(13)
O(25)	80(30)	82(17)	88(19)	-2(14)	-12(16)	-11(13)
C(26)	100(20)	90(20)	90(20)	-5(13)	-9(15)	-14(16)
C(27)	100(20)	60(20)	87(19)	-2(13)	-8(14)	-15(15)
O(28)	100(20)	70(30)	83(15)	-6(15)	0(13)	-18(13)
C(29)	110(20)	100(20)	60(20)	-17(14)	-7(14)	-22(16)
C(30)	110(30)	100(20)	82(19)	-18(18)	11(18)	-23(16)
O(31)	130(50)	120(30)	81(19)	-70(30)	40(20)	-33(18)
C(32)	90(30)	100(20)	53(15)	-40(20)	34(17)	-18(16)
C(33)	59(13)	65(18)	47(13)	-16(10)	12(10)	-3(12)
C(43)	70(20)	76(17)	99(18)	3(14)	-5(14)	-12(12)
C(44)	90(20)	70(18)	100(30)	5(17)	10(20)	-5(18)

O(45)	90(20)	69(15)	90(30)	5(13)	-9(17)	5(13)
C(46)	90(30)	66(14)	120(20)	-3(14)	10(17)	-1(13)
C(47)	80(20)	65(18)	140(30)	-6(15)	16(18)	12(17)
O(48)	75(19)	41(15)	130(30)	1(12)	19(16)	-1(14)
C(49)	80(20)	57(16)	160(30)	-9(13)	10(20)	21(18)
C(50)	71(19)	48(15)	160(50)	-7(11)	20(20)	19(18)
O(51)	66(17)	31(12)	140(40)	4(10)	5(19)	28(14)
C(52)	68(14)	24(12)	110(40)	6(9)	13(13)	24(14)
C(53)	70(14)	64(17)	79(18)	-5(10)	7(12)	17(14)
O(1S)	80(19)	90(20)	74(16)	-2(15)	-20(20)	10(30)

The anisotropic displacement factor exponent takes the form: $-2\pi^2[h^2a^{*2}U_{11} + ... + 2hka^*b^*U_{12}]$.

Table S3. Bond lengths [Å] for (DHT)$(H_3O)_2Bi_4I_{16}\cdot 2(H_2O)$ at 298.00 K with estimated standard deviations in parentheses.

Label	Distances
Bi(1)-I(3)	3.3684(17)
Bi(1)-I(3)#1	3.3684(17)
Bi(1)-I(4)#1	2.894(2)
Bi(1)-I(4)	2.894(2)
Bi(1)-I(5)	3.0763(14)
Bi(1)-I(5)#1	3.0763(14)
Bi(2)-I(1)	3.3520(19)
Bi(2)-I(3)	3.2528(9)
Bi(2)-I(5)	3.3008(18)
Bi(2)-I(6)	2.9528(12)
Bi(2)-I(7)	2.931(2)
Bi(2)-I(8)	2.920(2)
Bi(3)-I(1)#1	3.0896(13)
Bi(3)-I(1)	3.0897(13)
Bi(3)-I(2)	2.902(2)
Bi(3)-I(2)#1	2.902(2)
Bi(3)-I(3)	3.3344(17)
Bi(3)-I(3)#1	3.3344(17)
N(1)-H(1)	0.9800
N(1)-C(3)	1.45(2)
N(1)-C(23)	1.51(2)
N(1)-C(43)	1.47(2)
N(2)-H(2)	0.9800
N(2)-C(13)	1.55(2)
N(2)-C(33)	1.49(2)
N(2)-C(53)	1.53(2)

Symmetry transformations used to generate equivalent atoms:
(1) -x,-y+1,z

Table S4. Bond angles [°] for (DHT)$(H_3O)_2Bi_4I_{16}\cdot 2(H_2O)$ at 298.00 K with estimated standard deviations in parentheses.

Label	Angles
I(3)#1-Bi(1)-I(3)	82.27(5)
I(4)-Bi(1)-I(3)	90.82(6)
I(4)#1-Bi(1)-I(3)#1	90.82(6)
I(4)-Bi(1)-I(3)#1	172.63(7)
I(4)#1-Bi(1)-I(3)	172.63(7)
I(4)#1-Bi(1)-I(4)	96.18(11)
I(4)-Bi(1)-I(5)	89.85(6)
I(4)-Bi(1)-I(5)#1	91.87(6)
I(4)#1-Bi(1)-I(5)	91.87(6)
I(4)#1-Bi(1)-I(5)#1	89.85(6)
I(5)#1-Bi(1)-I(3)	92.20(4)
I(5)-Bi(1)-I(3)#1	92.20(4)
I(5)#1-Bi(1)-I(3)#1	85.86(3)
I(5)-Bi(1)-I(3)	85.86(3)
I(5)-Bi(1)-I(5)#1	177.42(7)
I(3)-Bi(2)-I(1)	84.47(4)
I(3)-Bi(2)-I(5)	84.22(4)
I(5)-Bi(2)-I(1)	91.47(4)
I(6)-Bi(2)-I(1)	86.45(5)
I(6)-Bi(2)-I(3)	167.86(4)
I(6)-Bi(2)-I(5)	87.98(5)
I(7)-Bi(2)-I(1)	89.12(6)
I(7)-Bi(2)-I(3)	92.20(5)
I(7)-Bi(2)-I(5)	176.30(5)
I(7)-Bi(2)-I(6)	95.71(6)
I(8)-Bi(2)-I(1)	175.52(5)
I(8)-Bi(2)-I(3)	91.16(5)
I(8)-Bi(2)-I(5)	87.09(6)
I(8)-Bi(2)-I(6)	97.74(7)
I(8)-Bi(2)-I(7)	92.05(5)
I(1)#1-Bi(3)-I(1)	172.47(8)
I(1)-Bi(3)-I(3)	87.36(4)
I(1)-Bi(3)-I(3)#1	87.02(4)
I(1)#1-Bi(3)-I(3)	87.02(4)
I(1)#1-Bi(3)-I(3)#1	87.36(4)
I(2)#1-Bi(3)-I(1)#1	93.15(6)

I(2)#1-Bi(3)-I(1)	91.90(6)
I(2)-Bi(3)-I(1)#1	91.90(6)
I(2)-Bi(3)-I(1)	93.15(6)
I(2)-Bi(3)-I(2)#1	95.66(10)
I(2)-Bi(3)-I(3)	173.77(7)
I(2)-Bi(3)-I(3)#1	90.53(5)
I(2)#1-Bi(3)-I(3)#1	173.77(7)
I(2)#1-Bi(3)-I(3)	90.53(5)
I(3)-Bi(3)-I(3)#1	83.29(5)
Bi(3)-I(1)-Bi(2)	95.15(4)
Bi(2)-I(3)-Bi(1)	92.64(4)
Bi(2)-I(3)-Bi(3)	92.49(3)
Bi(3)-I(3)-Bi(1)	97.22(2)
Bi(1)-I(5)-Bi(2)	97.29(4)
C(3)-N(1)-H(1)	100.1
C(3)-N(1)-C(23)	116(3)
C(3)-N(1)-C(43)	124(3)
C(23)-N(1)-H(1)	100.1
C(43)-N(1)-H(1)	100.1
C(43)-N(1)-C(23)	111(3)
C(13)-N(2)-H(2)	110.9
C(33)-N(2)-H(2)	110.9
C(33)-N(2)-C(13)	108(2)
C(33)-N(2)-C(53)	110(3)
C(53)-N(2)-H(2)	110.9
C(53)-N(2)-C(13)	105(3)
N(1)-C(3)-H(3A)	107.7
N(1)-C(3)-H(3B)	107.7
N(1)-C(3)-C(4)	118(3)
H(3A)-C(3)-H(3B)	107.1
C(4)-C(3)-H(3A)	107.7
C(4)-C(3)-H(3B)	107.7
C(3)-C(4)-H(4A)	110.3
C(3)-C(4)-H(4B)	110.3
H(4A)-C(4)-H(4B)	108.6
O(5)-C(4)-C(3)	107(3)
O(5)-C(4)-H(4A)	110.3
O(5)-C(4)-H(4B)	110.3

C(6)-O(5)-C(4)	114(3)
O(5)-C(6)-H(6A)	109.4
O(5)-C(6)-H(6B)	109.4
O(5)-C(6)-C(7)	111(3)
H(6A)-C(6)-H(6B)	108.0
C(7)-C(6)-H(6A)	109.4

Symmetry transformations used to generate equivalent atoms:
(1) -x,-y+1,z

Table S5. Atomic coordinates ($x10^4$) and equivalent isotropic displacement parameters ($Å^2x10^3$) for $(DHT)Bi_2I_8 \cdot 2(H_2O)$ at 296 K with estimated standard deviations in parentheses.

Label	x	y	z	Occupancy	U_{eq}^*
Bi(1)	1330(1)	6405(1)	9715(1)	1	44(1)
Bi(2)	1427(1)	2675(1)	8275(1)	1	49(1)
I(2)	-1370(1)	5660(1)	9590(1)	1	49(1)
I(1)	1276(1)	7907(1)	11694(1)	1	58(1)
I(5)	1252(1)	4818(1)	7742(1)	1	58(1)
I(3)	1120(1)	8110(1)	9050(1)	1	70(1)
I(4)	3691(1)	6992(1)	10101(1)	1	78(1)
I(6)	1419(1)	841(1)	8842(1)	1	76(1)
I(8)	1033(1)	1359(1)	6310(1)	1	82(1)
I(7)	3791(1)	3334(1)	8518(1)	1	84(1)
O(5)	6948(6)	8682(6)	5445(5)	1	63(2)
O(4)	7950(6)	8397(7)	6928(6)	1	70(2)
O(3)	5614(7)	5731(6)	7511(6)	1	70(2)
O(1)	1989(7)	4563(7)	4232(6)	1	75(2)
O(00F)	5561(8)	7640(7)	6516(6)	1	79(2)
H(00A)	5210(50)	8130(50)	6680(60)	1	119
H(00B)	6020(100)	7760(110)	6160(90)	1	119
O(2)	3166(7)	4902(6)	5926(5)	1	71(2)
O00H()	3910(8)	6344(8)	4948(6)	1	85(3)
H(00C)	3610(120)	5730(60)	4980(90)	1	128
H(00D)	4250(50)	6750(90)	5490(30)	1	128
N(2)	6813(8)	8065(7)	8293(6)	1	63(2)
H(2)	6380.42	7906.16	7700.33	1	76
O(6)	4486(7)	8441(7)	4121(6)	1	83(3)
O(9)	5420(7)	9454(8)	8173(6)	1	86(3)

O(8)	3695(8)	8560(8)	6731(6)	1	85(3)
O(7)	1591(8)	7281(7)	5402(6)	1	83(3)
N(1)	2510(8)	6502(8)	3624(6)	1	69(3)
H(1)	2931.9	6530.21	4181.12	1	82
C(11)	8570(10)	9024(10)	6472(8)	1	69(3)
H(11A)	8885.28	8567.57	5983	1	83
H(11B)	9158.34	9590.03	6903.85	1	83
C(2)	1246(10)	4875(11)	3743(9)	1	78(4)
H(2A)	922.73	5398.48	4167.21	1	93
H(2B)	663.81	4249.53	3376.67	1	93
C(10)	8576(9)	8315(11)	7649(9)	1	74(3)
H(10A)	8925.09	9032.44	8093.99	1	89
H(10B)	9142.93	7953.36	7417.98	1	89
C(16)	3311(11)	6745(10)	2986(8)	1	70(3)
H(16A)	2910.64	6480.54	2370.73	1	85
H(16B)	3850.75	6329.07	2967.65	1	85
C(14)	5479(10)	8184(10)	4251(8)	1	69(3)
H(14A)	5845.86	8108.14	3710.76	1	83
H(14B)	5353.9	7504.75	4353.2	1	83
C(7)	5977(10)	6274(9)	8467(8)	1	63(3)
H(7A)	6671.02	6128.55	8610.31	1	76
H(7B)	5453.89	5975.11	8801.08	1	76
C(4)	2427(11)	3893(10)	5366(9)	1	77(4)
H(4A)	2130.21	3494.7	5744.8	1	92
H(4B)	2805.49	3453.86	4920.7	1	92
C(24)	7080(11)	9283(10)	8800(9)	1	78(4)
H(24A)	7481.08	9637.12	8429.7	1	94
H(24B)	7552.93	9468.87	9372.23	1	94
C(9)	7842(10)	7685(11)	8090(10)	1	77(4)
H(9A)	8237.01	7738.29	8660.69	1	93
H(9B)	7640.69	6927.18	7688.52	1	93
C(8)	6118(11)	7458(11)	8800(8)	1	77(4)
H(8A)	6438.32	7758.9	9442.14	1	92
H(8B)	5397.71	7598.59	8772.32	1	92
C(5)	4087(12)	4742(11)	6371(8)	1	82(4)
H(5A)	4654.14	4674.32	5975.97	1	98
H(5B)	3879.39	4080.2	6498.27	1	98
C(12)	7790(10)	9515(9)	6082(8)	1	68(3)

H(12A)	7475.73	9967.02	6575.19	1	82
H(12B)	8183.26	9966.7	5778.25	1	82
C(23)	6064(12)	9718(11)	9016(9)	1	84(4)
H(23A)	5659.8	9388	9400.38	1	101
H(23B)	6274.97	10497.67	9339.56	1	101
C(6)	4508(10)	5687(10)	7251(8)	1	70(3)
H(6A)	4458.35	6352.39	7166.21	1	83
H(6B)	4075.39	5605	7727.07	1	83
C(15)	3922(11)	7926(10)	3219(10)	1	80(4)
H(15A)	4442.09	7956.41	2788.81	1	96
H(15B)	3399.88	8326.78	3134	1	96
C(13)	6177(11)	9091(10)	5080(10)	1	82(4)
H(13A)	6548.83	9679.38	4900.69	1	98
H(13B)	5721.36	9369.51	5538.7	1	98
C(1)	1849(11)	5367(10)	3131(8)	1	76(4)
H(1A)	2330.59	4923.28	2838.44	1	91
H(1B)	1323.48	5358.1	2650.47	1	91
C(18)	1990(12)	7952(11)	4910(9)	1	76(3)
H(18A)	2767.07	8277.2	5110.11	1	91
H(18B)	1615.72	8529.49	5027.41	1	91
C(3)	1540(12)	4145(11)	4890(9)	1	82(4)
H(3A)	956.87	3494.22	4584.45	1	98
H(3B)	1239.39	4675.89	5329.34	1	98
C(17)	1797(12)	7284(11)	3907(8)	1	81(4)
H(17A)	1922.47	7764.65	3564.86	1	97
H(17B)	1036.08	6878.13	3739.1	1	97
C(19)	1715(11)	7817(14)	6377(9)	1	100(5)
H(19A)	1114.7	7455.53	6610.66	1	121
H(19B)	1657.91	8555.65	6511.88	1	121
C(20)	2779(12)	7845(13)	6882(9)	1	91(4)
H(20A)	2732.01	8074.59	7535.6	1	110
H(20B)	2892.84	7119.69	6680.13	1	110
C(22)	4442(13)	9825(14)	8268(11)	1	111(6)
H(22A)	4614.07	10588.36	8651.3	1	134
H(22B)	3946.42	9424.26	8555.03	1	134
C(21)	3924(14)	9653(14)	7336(12)	1	107(5)
H(21A)	3247.02	9884.27	7387.15	1	129
H(21B)	4406.94	10100.95	7076.91	1	129

*U_{eq} is defined as one third of the trace of the orthogonalized U_{ij} tensor.

Table S6. Anisotropic displacement parameters ($Å^2x10^3$) for (DHT)Bi_2I_8·2(H_2O) at 296 K with estimated standard deviations in parentheses.

Label	U_{11}	U_{22}	U_{33}	U_{12}	U_{13}	U_{23}
Bi(1)	47(1)	42(1)	43(1)	11(1)	2(1)	16(1)
Bi(2)	55(1)	47(1)	46(1)	15(1)	4(1)	17(1)
I(2)	52(1)	50(1)	45(1)	12(1)	-2(1)	18(1)
I(1)	57(1)	64(1)	44(1)	13(1)	-1(1)	9(1)
I(5)	72(1)	56(1)	44(1)	18(1)	3(1)	16(1)
I(3)	90(1)	60(1)	70(1)	21(1)	7(1)	38(1)
I(4)	48(1)	78(1)	93(1)	12(1)	4(1)	16(1)
I(6)	92(1)	59(1)	85(1)	19(1)	-2(1)	38(1)
I(8)	104(1)	75(1)	48(1)	3(1)	16(1)	11(1)
I(7)	55(1)	97(1)	100(1)	18(1)	6(1)	37(1)
O(5)	72(5)	56(4)	53(4)	6(4)	-6(4)	17(3)
O(4)	46(4)	91(6)	75(5)	-1(4)	-7(4)	47(5)
O(3)	61(5)	72(5)	74(5)	18(4)	4(4)	25(4)
O(1)	63(5)	90(6)	70(5)	14(4)	-2(4)	32(5)
O(00F)	75(6)	92(6)	62(5)	9(5)	5(4)	24(5)
O(2)	77(6)	63(5)	67(5)	11(4)	-11(4)	21(4)
O00H()	78(6)	92(7)	80(6)	-2(5)	-11(5)	43(5)
N(2)	65(6)	62(6)	63(6)	7(4)	2(5)	29(5)
O(6)	66(6)	71(6)	88(6)	10(4)	-9(5)	6(5)
O(9)	72(6)	96(7)	67(5)	22(5)	-2(5)	0(5)
O(8)	85(7)	104(7)	56(5)	25(5)	8(5)	16(5)
O(7)	85(6)	85(6)	63(5)	6(5)	-2(5)	19(4)
N(1)	77(7)	77(7)	49(5)	29(5)	-9(5)	17(5)
C(11)	63(8)	73(8)	61(7)	0(6)	1(6)	23(6)
C(2)	59(8)	80(9)	84(9)	-4(6)	-7(7)	32(7)
C(10)	43(6)	101(10)	83(9)	3(6)	-3(6)	49(8)
C(16)	83(9)	74(8)	54(7)	24(7)	3(6)	22(6)
C(14)	70(8)	66(7)	63(7)	27(6)	-11(6)	13(6)
C(7)	59(7)	73(8)	63(7)	21(6)	14(6)	27(6)
C(4)	95(10)	65(8)	61(7)	8(7)	-10(7)	21(6)
C(24)	73(9)	70(8)	72(8)	-3(6)	-23(7)	19(6)
C(9)	61(8)	101(10)	88(9)	25(7)	15(7)	53(8)

C(8)	79(9)	91(9)	52(7)	10(7)	10(6)	21(6)
C(5)	105(11)	79(9)	56(7)	36(8)	-5(7)	11(6)
C(12)	70(8)	63(7)	60(7)	3(6)	-6(6)	18(5)
C(23)	94(11)	71(8)	70(9)	21(7)	-8(8)	6(6)
C(6)	69(8)	72(8)	66(7)	16(6)	-1(6)	26(6)
C(15)	75(9)	69(8)	87(9)	1(6)	-9(7)	31(7)
C(13)	84(9)	57(7)	93(10)	8(6)	-26(8)	24(7)
C(1)	89(10)	66(8)	59(7)	14(7)	-9(7)	11(6)
C(18)	87(10)	76(8)	73(8)	24(7)	23(7)	34(7)
C(3)	90(10)	77(9)	67(8)	2(7)	3(7)	26(7)
C(17)	95(10)	96(10)	59(7)	40(8)	4(7)	28(7)
C(19)	67(9)	155(15)	56(8)	7(9)	8(7)	21(9)
C(20)	85(10)	119(12)	62(8)	14(9)	11(7)	29(8)
C(22)	86(11)	109(13)	100(12)	27(9)	-7(9)	-9(9)
C(21)	99(12)	120(14)	104(13)	39(10)	0(10)	38(11)

The anisotropic displacement factor exponent takes the form: $-2\pi^2[h^2a^{*2}U_{11} + ... + 2hka^*b^*U_{12}]$.

Table S7. Bond lengths [Å] for (DHT)$Bi_2I_8 \cdot 2(H_2O)$ at 296 K with estimated standard deviations in parentheses.

Label	Distances
Bi(1)-I(2)	3.3170(8)
Bi(1)-I(2)#1	3.3434(7)
Bi(1)-I(1)	3.0783(7)
Bi(1)-I(5)	3.0748(7)
Bi(1)-I(3)	2.8955(8)
Bi(1)-I(4)	2.8882(9)
Bi(2)-I(2)#1	3.3395(7)
Bi(2)-I(1)#1	3.3408(8)
Bi(2)-I(5)	3.3328(8)
Bi(2)-I(6)	2.9130(8)
Bi(2)-I(8)	2.9228(9)
Bi(2)-I(7)	2.8904(10)
O(5)-C(12)	1.411(13)
O(5)-C(13)	1.404(14)
O(4)-C(11)	1.426(13)
O(4)-C(10)	1.391(13)
O(3)-C(7)	1.418(13)
O(3)-C(6)	1.416(14)
O(1)-C(2)	1.399(15)
O(1)-C(3)	1.424(15)

Symmetry transformations used to generate equivalent atoms:
(1) -x,-y+1,-z+2

Table S8. Bond angles [°] for (DHT)$Bi_2I_8 \cdot 2(H_2O)$ at 296 K with estimated standard deviations in parentheses.

Label	Angles
I(2)-Bi(1)-I(2)#1	85.922(18)
I(1)-Bi(1)-I(2)#1	91.10(2)
I(1)-Bi(1)-I(2)	85.30(2)
I(5)-Bi(1)-I(2)	91.53(2)
I(5)-Bi(1)-I(2)#1	87.286(19)
I(5)-Bi(1)-I(1)	176.55(2)
I(3)-Bi(1)-I(2)#1	175.54(2)
I(3)-Bi(1)-I(2)	89.91(2)
I(3)-Bi(1)-I(1)	90.16(2)
I(3)-Bi(1)-I(5)	91.23(2)
I(4)-Bi(1)-I(2)	170.69(3)
I(4)-Bi(1)-I(2)#1	87.20(2)
I(4)-Bi(1)-I(1)	88.57(2)
I(4)-Bi(1)-I(5)	94.40(2)
I(4)-Bi(1)-I(3)	97.12(3)
I(2)#1-Bi(2)-I(1)#1	80.960(18)
I(5)-Bi(2)-I(2)#1	83.291(18)
I(5)-Bi(2)-I(1)#1	89.53(2)
I(6)-Bi(2)-I(2)#1	93.07(2)
I(6)-Bi(2)-I(1)#1	86.13(2)
I(6)-Bi(2)-I(5)	174.74(3)
I(6)-Bi(2)-I(8)	94.06(3)
I(8)-Bi(2)-I(2)#1	167.15(3)
I(8)-Bi(2)-I(1)#1	88.87(2)
I(8)-Bi(2)-I(5)	88.83(2)
I(7)-Bi(2)-I(2)#1	91.34(3)
I(7)-Bi(2)-I(1)#1	172.14(3)
I(7)-Bi(2)-I(5)	91.12(3)
I(7)-Bi(2)-I(6)	92.77(3)
I(7)-Bi(2)-I(8)	98.97(3)
Bi(1)-I(2)-Bi(1)#1	94.078(18)
Bi(1)-I(2)-Bi(2)#1	94.553(18)
Bi(2)#1-I(2)-Bi(1)#1	92.062(18)
Bi(1)-I(1)-Bi(2)#1	99.17(2)
Bi(1)-I(5)-Bi(2)	97.21(2)
C(13)-O(5)-C(12)	112.2(9)

C(10)-O(4)-C(11)	113.0(9)
C(6)-O(3)-C(7)	113.7(9)
C(2)-O(1)-C(3)	114.5(10)

Symmetry transformations used to generate equivalent atoms:
(1) -x,-y+1,-z+2

SEM studies

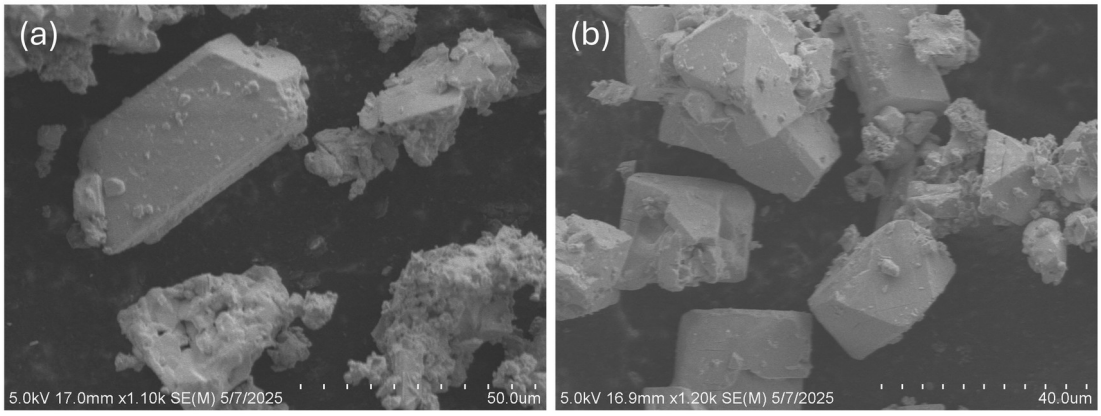

Figure S6. Representative SEM images of the fresh sample.

EDS measurements

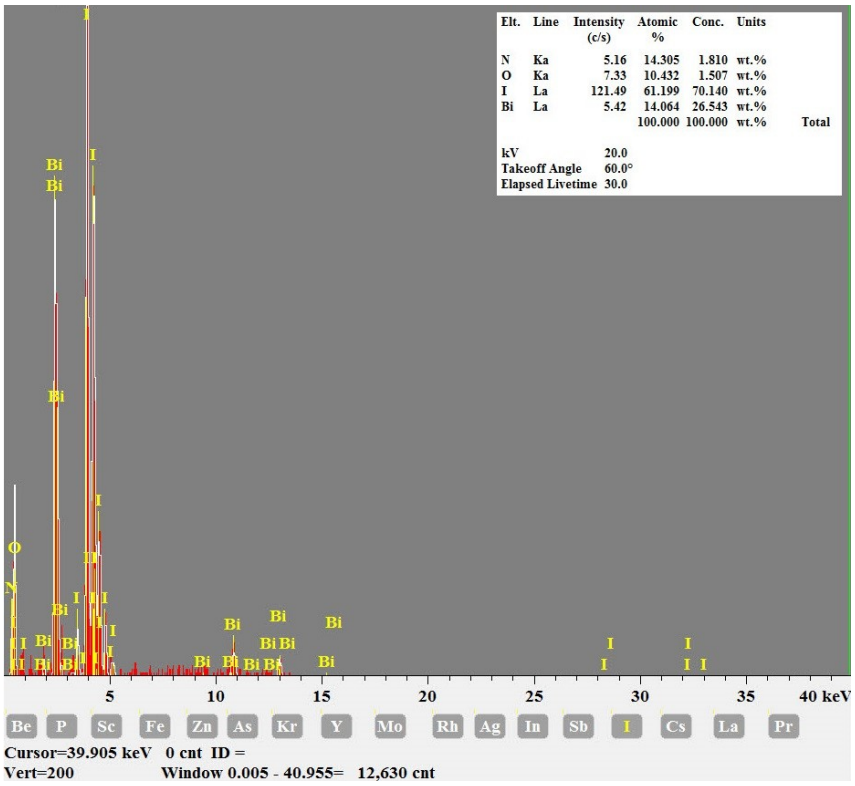

Figure S7. Representative EDS spectrum of fresh crystals. The Bi:I ratio is 1:4.3, matching closely the formula derived from XRD studies.

Thermogravimetric analysis

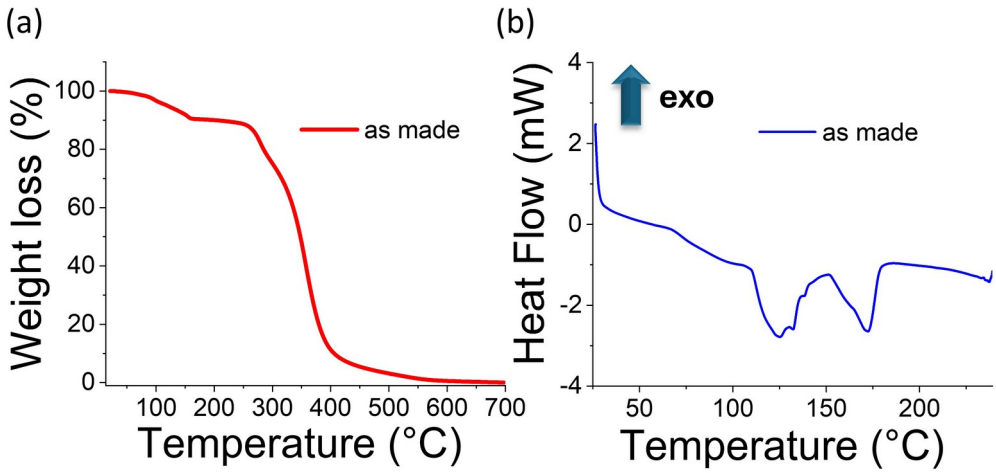

Figure S8. a) TGA curve for the dried as-made crystals, b) DSC curve for the dried as-made crystals exhibiting two endothermic peaks.

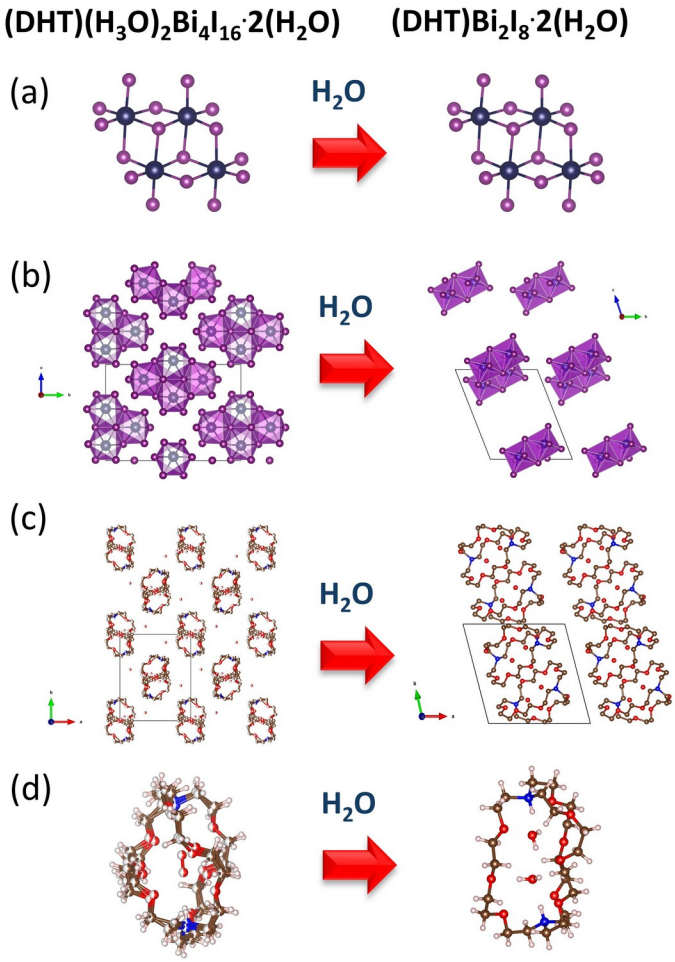

Figure S9. Comparison among the as made $(DHT)(H_3O)_2Bi_4I_{16}\cdot 2(H_2O)$ and the SCSC phase that formed after the water treatment, $(DHT)Bi_2I_8\cdot 2(H_2O)$ in terms of the a) inorganic clusters, b) structural configuration of inorganic and c) organic parts as well as d) configuration of individual ligands. In the latter case, the disorder is lifted, and there are only H_2O molecules residing in the cage cavities.

PXRD studies

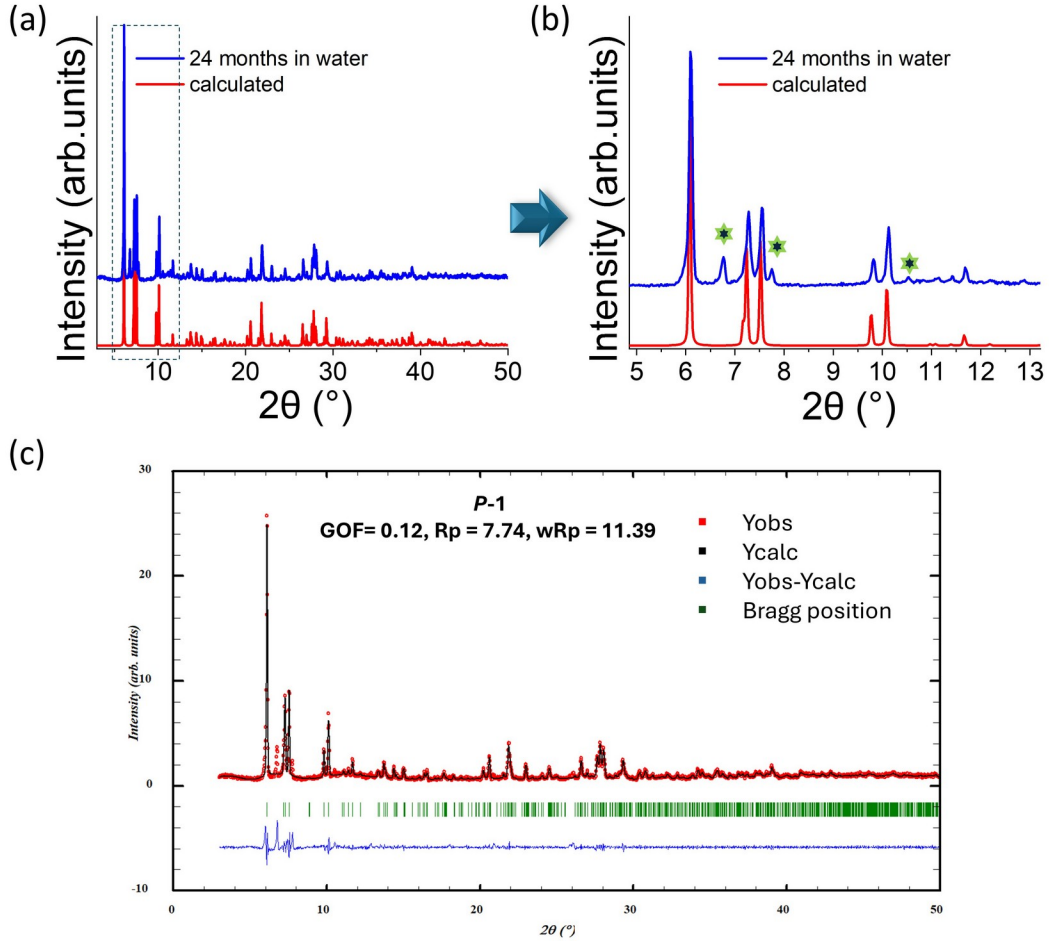

Figure S10. a, b) Comparison of experimental and calculated PXRD patterns for the water treated material (DHT)Bi_2I_8·2(H_2O), the green asterisk indicates the position of the diffraction peaks of a secondary unknown phase. c) Observed and calculated diffraction profiles from the Le Bail fitting method of the (DHT)Bi_2I_8·2(H_2O) material.

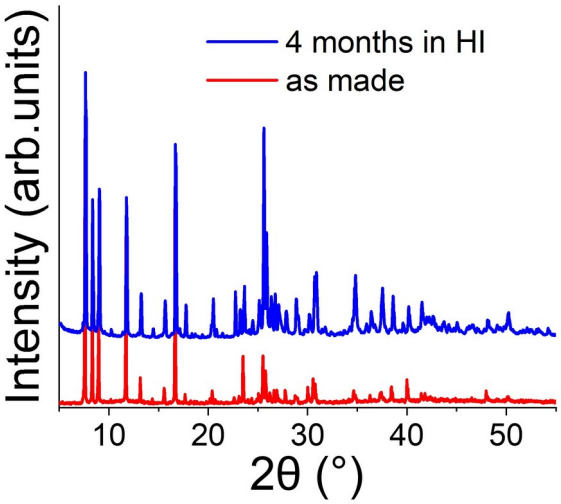

Figure S11. Comparison of experimental PXRD patterns for the freshly made material and the 4 months in HI one. The material maintains its structural integrity in strongly acidic conditions.

DFT Studies

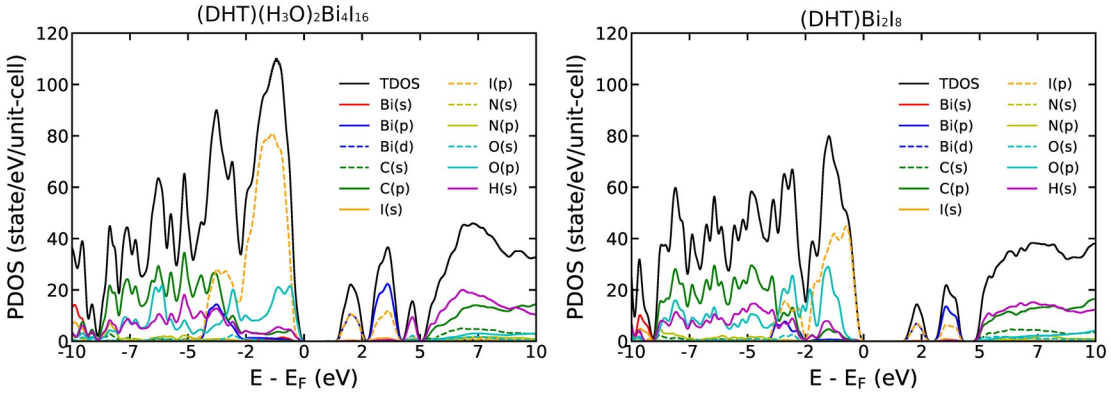

Figure S12. Total and partial density of states of $(DHT)(H_3O)_2Bi_4I_{16}$ and $(DHT)Bi_2I_8$.

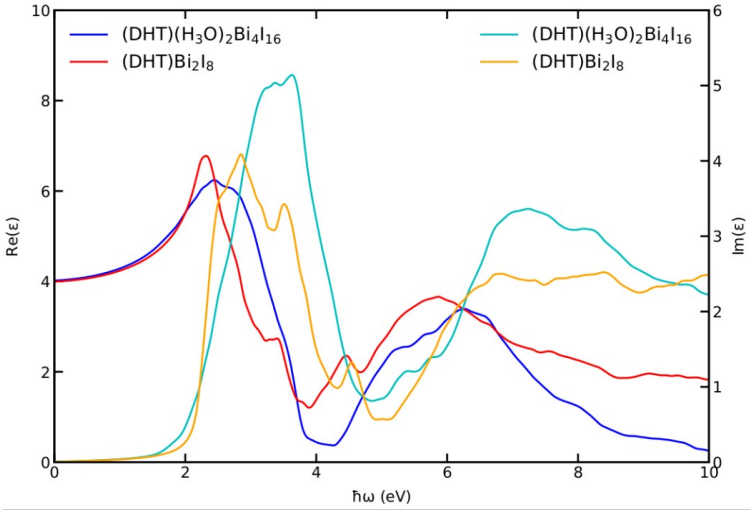

Figure S13. Real (red and blue) and imaginary parts (cyan and orange) of the dielectric functions of $(DHT)(H_3O)_2Bi_4I_{16}$ and $(DHT)Bi_2I_8$.

TRPL measurements

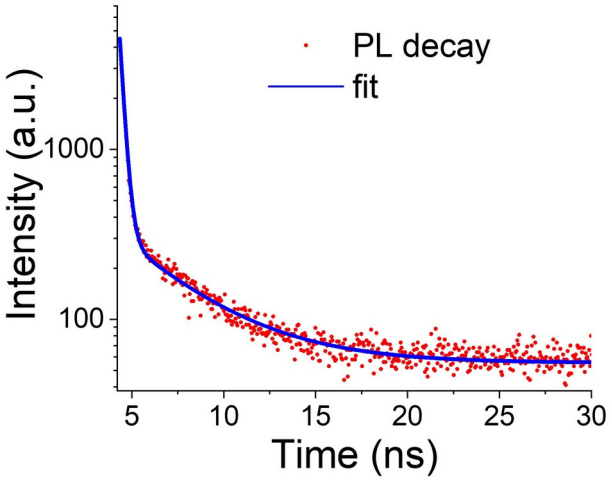

Figure S14. Time-resolved photoluminescence decay of (DHT)$(H_3O)_2Bi_4I_{16}$·$2(H_2O)$ at 298 K.

ROS studies

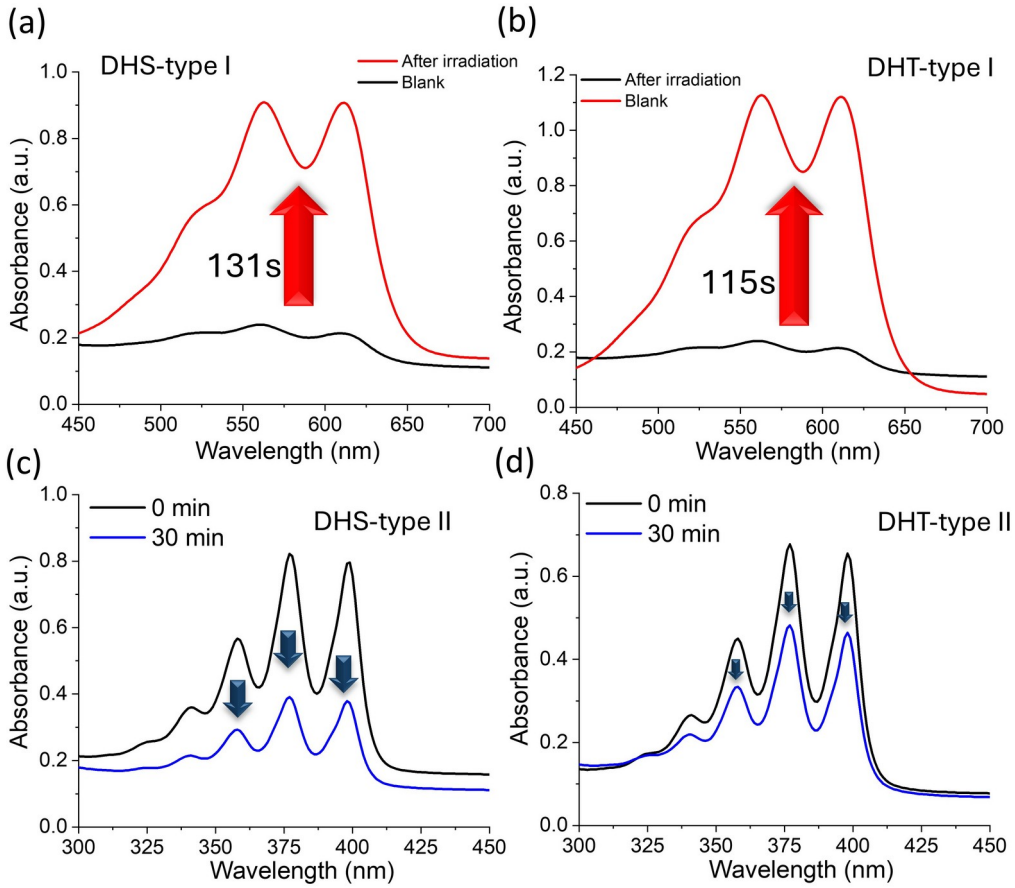

Figure S15. Type-I ROS generation by a) (DHS)Bi_2I_8 over 131s and b) (DHT) $(H_3O)_2Bi_4I_{16}$·$2(H_2O)$ over 115s. Type-II ROS generation by c) (DHS)Bi_2I_8 showing a 56% degradation of ABDA, and d) (DHT)$(H_3O)_2Bi_4I_{16}$·$2(H_2O)$ showing a 33% degradation of ABDA.

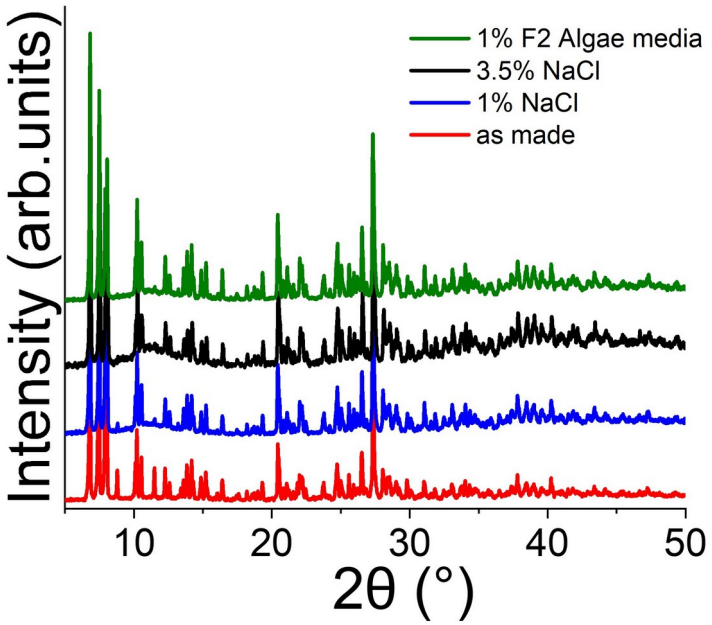

Figure S16. Comparison of the experimental PXRD patterns for the as-made crystals to those treated with 1% NaCl, 3.5% NaCl, and 1% F/2 algae growth medium for 24h.

Table S9. Comparison of common algicidal agents for the mitigation of *K. brevis*, with specific attention on ROS-based compounds.

Treatment type	Inhibition concentration
dibutyl phthalate (DBP)	5 mg/L[1]
Calcium Peroxide	8 mg H_2O_2/L[2-3]
PAK® 27	6.48 mg H_2O_2/L[2]
Oximycin® P5	7.08 mg H_2O_2/L[2]
Algimycin® PWF	1 mg Cu/L[2]

S4. References

1. Li, F.-m.; Wu, M.; Yao, Y.; Zheng, X.; Zhao, J.; Wang, Z.-y.; Xing, B.-s., Inhibitory effects and oxidative target site of dibutyl phthalate on Karenia brevis, *Chemosphere* **2015,** *132*, 32-39.
2. Hu, J.; Berthold, D. E.; Wang, Y.; Xiao, X.; Laughinghouse, H. D., Treatment of the red tide dinoflagellate Karenia brevis and brevetoxins using USEPA-registered algaecides, *Harmful Algae* **2022,** *120*, 102347.
3. Hossain, I.; Mays, B.; Hanhart, S. L.; Hubble, J.; Azizihariri, P.; McLean, T. I.; Pierce, R.; Lovko, V.; John, V. T., An effective algaecide for the targeted destruction of Karenia brevis, *Harmful Algae* **2024,** *138*, 102707.